Cellular compartmentalisation and receptor promiscuity as a strategy for accurate and robust inference of position during morphogenesis

Krishnan S Iyer* and Madan Rao†
Simons Center for the Study of Living Machines,
National Center for Biological Sciences - TIFR, Bangalore 560065, India

Chaitra Prabhakara and Satyajit Mayor
National Center for Biological Sciences - TIFR, Bangalore 560065, India
(Dated: March 30, 2022)

Precise spatial patterning of cell fate during morphogenesis requires accurate inference of cellular position. In making such inferences from morphogen profiles, cells must contend with inherent stochasticity in morphogen production, transport, sensing and signalling. Motivated by the multitude of signalling mechanisms in various developmental contexts, we show how cells may utilise multiple tiers of processing (compartmentalisation) and parallel branches (multiple receptor types), together with feedback control, to bring about fidelity in morphogenetic decoding of their positions within a developing tissue. By simultaneously deploying specific and nonspecific receptors, cells achieve a more accurate and robust inference. We explore these ideas in the patterning of *Drosophila melanogaster* wing imaginal disc by Wingless morphogen signalling, where multiple endocytic pathways participate in decoding the morphogen gradient. This distributed information processing at the scale of the cell highlights how local cell autonomous control facilitates global tissue scale design.

Keywords: morphogenetic decoding, positional inference, cellular compartmentalisation, receptor promiscuity, Bayesian inference, feedback control

* Correspondence email address: iyersk@ncbs.res.in
† Correspondence email address: rao.madan@gmail.com

I. INTRODUCTION

Precise positioning of cell fates and cell fate boundaries in a developing tissue is of vital importance in ensuring a correct developmental path (reviewed in [1, 2]). The required positional information is often conveyed by concentration gradients of secreted signalling molecules, or morphogens (reviewed in [3, 4]). Typically, a spatially varying input morphogen profile is translated into developmentally meaningful transcriptional outputs. Morphogen profile measurements, across several signalling contexts, show that the gradients are inherently noisy [5–9]. However, positional precision of the signaling output should be robust to inherent genetic or environmental fluctuations in the concentrations of the ligands and receptors engaged in translating the positional information. For example, the noisy profile of the morphogen Bicoid (Bcd) that activates hunchback (hb) in the early Drosophila embryo [6, 10], and the expression of gap genes that activate pair-rule genes [11, 12] result in cell fate boundaries that are positioned to a remarkable accuracy of about one cell's width. This points to a local, cell-autonomous morphogenetic decoding that is precise and robust to various sources of noise [13–15].

Cell-autonomous decoding of noisy morphogen profiles includes reading of morphogen concentration, followed by cellular processing, finally leading to inference in the form of transcriptional readout. Several strategies have been proposed to ensure precision in output (reviewed in [16, 17]): feedbacks such as self-enhanced morphogen degradation [18, 19], spatial and temporal averaging [6], use of two opposing gradients [20], pre-steady state patterning [21] and serial transcytosis [22].

Most cell signalling systems have regulatory mechanisms that fine-tune signalling by controlling ligand-specific receptor interactions [23]. Ligands such as TGFβ/BMP [24], Wnt [25], Notch [26], show promiscuous interactions with different receptors. Secreted inhibitors [27, 28] or sequestering components within the extra-cellular matrix [29] or interactions with binding receptors such as heparin sulphate proteoglycans (HSPGs) [30–32] can control availability of the ligand. Additionally, the multiple endocytic pathways that operate at the plasma membrane can control the extent of signalling [33, 34]. These examples argue for *distributed information processing* within the cell.

In this paper, we show how cellular compartmentalisation, a defining feature of multicellularity, provides a compelling realisation of such distributed cellular inference. We show that compartmentalisation together with multiple receptors, receptor promiscuity and feedback control, ensure precision and robustness in positional inference from noisy morphogen profiles during development. Compartments associated with specific chemical (e.g., lipids, proteins/enzymes) and physical (e.g., pH) environments, have been invoked as regulators of biochemical reactions during cellular signalling and development [33, 35–38]. Deploying promiscuous receptors against a morphogen in addition to its specific receptor, is a strategy to buffer variations in morphogen levels. These observations provide the motivation for a general conceptual framework for *morphogenetic decoding* based on a multi-tiered, multi-branched information channel. While our framework has broader applicability, we will, for clarity, use the terminology of Wingless signalling in *Drosophila* wing imaginal disc [39].

II. CONCEPTUAL FRAMEWORK AND QUANTITATIVE MODELS

We pose the task of morphogenetic decoding as a problem in local, cell autonomous inference of position from a morphogen input (Fig. 1), where each cell acts as an information/inference channel with the following information flow:

1. "reading" of the morphogen input by receptors on the cell surface,
2. "processing" by various cellular mechanisms such as receptor trafficking, secondary messengers, feedback control, and
3. "inference" of the cell's position in the form of a transcriptional readout.

At a phenomenological level, *reading* of the morphogen input is associated with the binding of the morphogen ligand to various receptors with varying degree of specificity, leading to the notion that the information channel describing positional inference must possess *multiple branches*. Furthermore, the multiple *processing* steps associated with compartmentalisation of cellular biochemistry and/or signal transduction modules, e.g. phosphorylation states, provide the motivation for invoking *multiple tiers* in the channel architecture. At an abstract level, one may think of the branch-tier architecture of the cellular processing as a bipartite Markovian network/graph [40], with a *fast* direction (involving multiple branches) consisting of ligand-bound and unbound states along with chemical

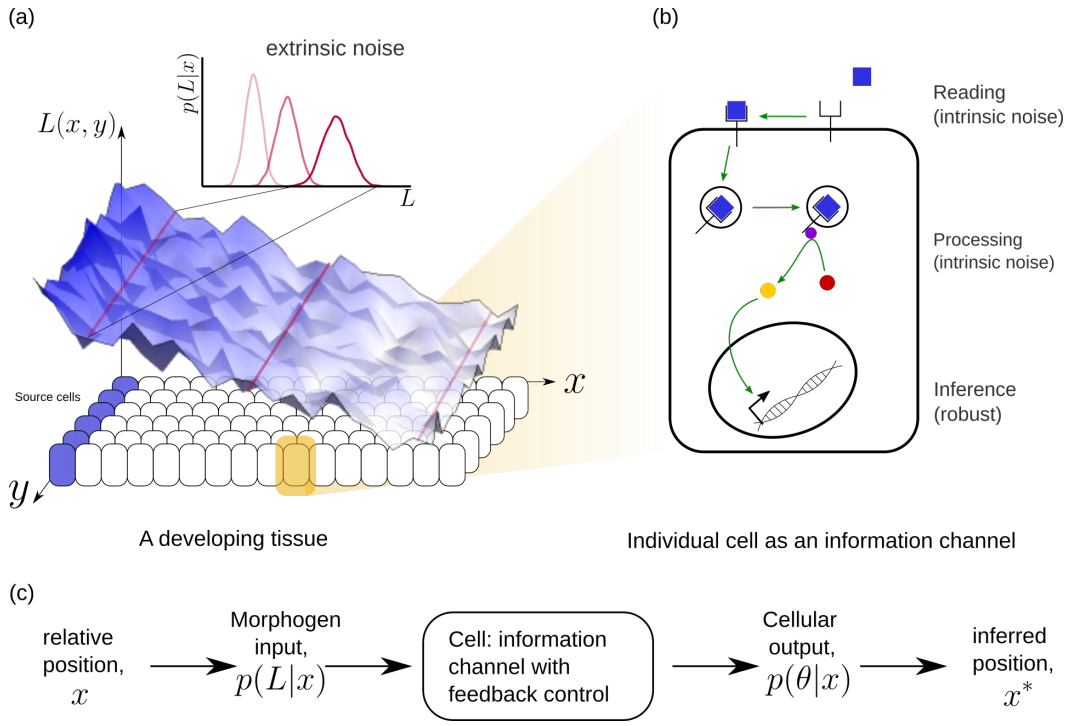

Figure 1. **(a)** Schematic of information processing in the developing tissue: a morphogen is produced by a specific set of cells (blue), and secreted into the lumen surrounding the tissue. Due to stochasticity of the production and transport processes, the morphogen concentration received by the rest of the cells is contaminated by *extrinsic noise*, which defines a distribution of morphogen concentration along the y-direction at any position x. **(b)** The route from morphogens to a developmental outcome requires each cell to read, process and infer its position. This task is further complicated by the stochasticity of the reading and processing steps themselves, that lead to *intrinsic noise*. **(c)** The problem of robust inference of position can be considered in a channel framework. The positional information is noisily encoded in the local morphogen (ligand) concentrations, $p(L|x)$. The cells receive this as input and process it into a less noisy output to ensure robustness in inferred positions.

state changes, and a *slower* direction (involving multiple tiers) characterised by energy-utilising processes or a flux imbalance. A general developmental context with multiple morphogens may involve several such bipartite Markov networks/graphs with different receptors (or branches) in parallel. Some of these receptors could be shared between different morphogens. We refer to these receptors as non-specific while the receptors that bind only to one morphogen are specific. At the end of processing, each individual cell may pool information from the various branches for the final inference of position, i.e. a transcriptional readout (Fig. 2).

The task of achieving a precise inference is complicated by the noise in morphogen input arising from both production and transport processes, and by the stochasticity of the reading and processing steps; thus the *inference* must be robust to the *extrinsic* and *intrinsic* sources of noise. The use of feedback control mechanisms is a common strategy to bring about robustness in the context of morphogen gradient formation and sensing [41]. Motivated by this, we consider different feedback controls (see Fig. 5) in conjunction with the tiers and branches. With these three elements to the channel architecture, the task of morphogenetic decoding can be summarised in the following objective.

Objective: Given a noisy input distribution at position x, i.e. $p(L|x)$, what are the requirements of the reading (number of receptor types and receptor concentrations) and processing steps (number of tiers and feedback type) such that the positional inference is precise and robust to extrinsic and intrinsic noise?

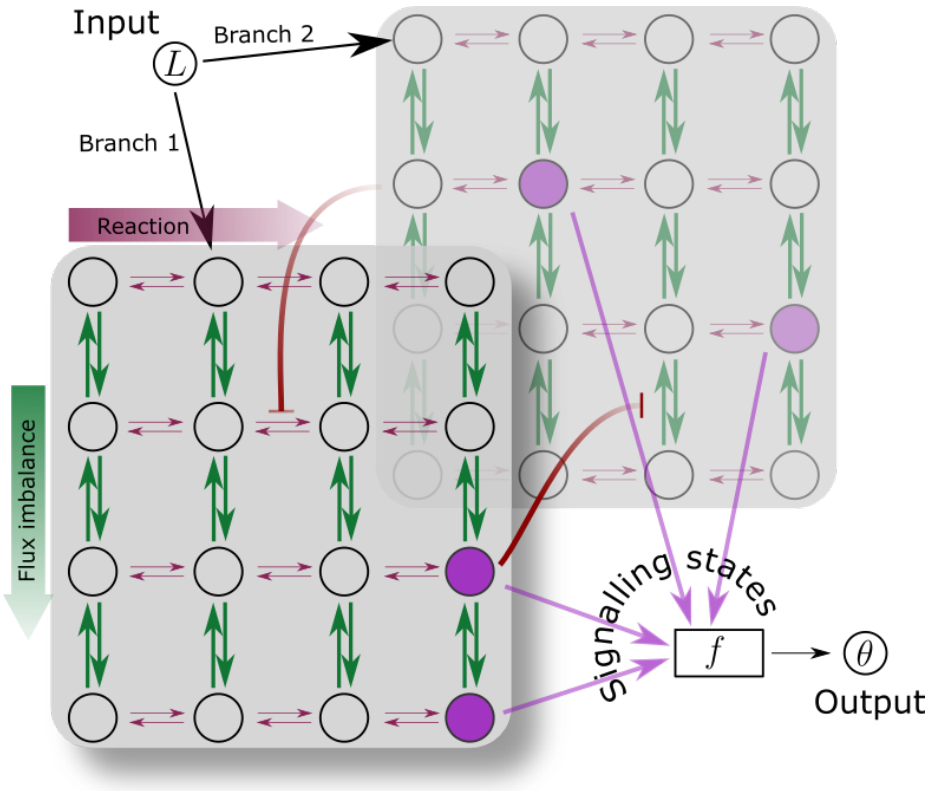

Figure 2. Schematic for the branch-tier channel architecture. Cellular processing associated with each receptor type, i.e. along each branch, is depicted by a bipartite Markov network. The horizontal arrows correspond to faster transitions between receptor states, e.g. bound/unbound, and vertical arrows depict slower transitions involving driven, flux-imbalanced processes, e.g. intracellular transport or phosphorylation. There may exist several feedback control loops (red ⟞ arrows) in the network. Ligand concentration L drives one or several reaction rates in such Markov networks as in [42]. The output θ is a collection f of several signalling states (purple nodes) from one or many branches. The statistics of the output then enables inference of ligand concentration and thus position.

A. Mathematical Framework

Figure 1 describes information processing during development across a two dimensional tissue of n_x, n_y cells in x and y directions, respectively. The direction of morphogen gradient is taken to be along x, with the morphogen source to the left of $x = 0$. Each cell is endowed with a chemical reaction network (CRN) with the same multi-tiered, multi-branched architecture with feedbacks described previously, that reads a noisy input $L(x, y)$ (morphogen concentration) and produces an "output" (biochemical "signal") $\theta(x, y)$ that is also noisy. Here we choose to construct the noisy morphogen profile in the following manner: for a given position $x \in [0, 1]$, cells along the y-direction see different amounts of ligand coming from the same *input distribution* $p(L|x)$,

$$p(L|x) = \frac{2}{\sqrt{2\pi\sigma_L^2(x)}} \mathrm{Exp}\left[-\frac{(L-\mu_L(x))^2}{2\sigma_L^2(x)}\right]\left(1 + \mathrm{Erf}\left[\frac{\mu_L(x)}{\sqrt{2}\sigma_L(x)}\right]\right)^{-1}. \tag{1}$$

characterised parametrically by $\mu_L(x)$ and $\sigma_L(x)$. Experimental data can be fit to this distribution Eq. 1 (or another distribution suitable for the specific experimental system) to obtain the parameters. Here, we consider an exponentially decaying mean μ_L and standard deviation σ_L

$$\mu_L(x) = Ae^{-x/\lambda} \tag{2}$$

$$\sigma_L(x) = \sqrt{\mu_L(x)} \tag{3}$$

but ofcourse any choice consistent with experimental observations would do. The values of A, λ chosen for our analysis are listed in Table. I. The corresponding output distribution $p(\theta|x)$ can be used to infer the cell's position. Since we do not know the precise functional relationship between the output and inferred position, we invoke Bayes Rule [43], as in previous work [44], to infer the cell's position,

$$p(x|\theta) = \frac{p(\theta|x)p(x)}{p(\theta)} \tag{4}$$

where $p(\theta) = \int_0^1 dx\, p(\theta|x)\, p(x)$ and $p(x)$ is the prior distribution which we take to be uniform over a tissue of unit length, $p(x) = 1$. We quantify precision in the inference by the **local inference error**, $\sigma_X(x)$. For each position x, the inferred position x^* of cells along the y-direction is given by the *maximum a posteriori* estimate,

$$x^*(x, y) = \underset{x}{\operatorname{argmax}}\, p(x|\theta(x, y)) \tag{5}$$

from which the **local** and **average inference error** can be computed

$$\sigma_X(x) = \langle (x^* - x)^2 \rangle_y \tag{6}$$

$$\bar{\sigma}_X = \int_0^1 \sigma_X(x)\, p(x)\, dx \tag{7}$$

where the average in Eq. 6 is over cells in the y-direction. The logic behind this definition of the inference error is that development of the tissue relies on the precision in the inference of cells' positions *throughout the tissue.* However, there may be tissue developmental contexts, where only the positions of certain *regions* or *cell fate boundaries* need to be specified with any precision (as in the case of short-range morphogen gradients like Nodal [45]). The definition of inference error may be readily extended to incorporate such specifications.

B. Quantitative models for cellular reading and processing

In order to calculate the probability of the inferred position given the output $p(x^*|\theta)$ and hence the inference error $\bar{\sigma}_X$, one needs to know the prior $p(x)$ and the input-output relation giving rise to the output distribution $p(\theta|x)$ in Eq. 4. While a uniform prior may be justified by a homogeneous distribution of cells in the developing tissue at the stage considered, the input-output relation needs to be developed using a specific model based on the general channel design principles described previously. Thus we will take each cell to be equipped with a chemical reaction network (CRN) that has up to two receptor types both of which bind the ligand on the cell surface but only one is signalling competent [3, 39]. This latter aspect breaks the symmetry between the receptor types and hence the branches, a point that we will revisit in Section III C. In multi-tier architecture, the bound states of both the receptors are internalised and shuttled through several compartments. The last compartment allows for a conjugation reaction between the two receptors (as in the case of Wingless and Dpp [39, 46]). The signalling states are defined by all the bound states of the signalling receptor contribute to the output. Within this schema, we consider control mechanisms on the surface receptor concentrations and in the chemical reactions downstream to binding on the surface (i.e. on internalisation, shuttling, conjugation, etc). We formulate the control on processing steps as a feedback/feedforward regulation from one of the signalling species in the CRN. On the other hand, the control of surface receptors is considered in the form of an open-loop control by allowing receptor profiles to vary within certain bounds (see Table I). The key parameters are *chemical rate parameters* describing the rates of various reactions in the CRN, *receptor parameters* describing the receptor concentration profiles, *feedback topology* in the CRN i.e. a combination of actuator and rate under regulation, *control parameters* describing the strength and sensitivity of the feedback/feedforward. With these parameters specified, an input-output relation, calculated as a tier-wise weighted sum of all signalling states, can then be used to infer the cell's position by Eq. 4.

Cellular Reading via surface receptors. In the framework described previously, we consider the morphogen ligand as an *external input* to the receiving cells, outside the cellular information processing channel. The signal and noise therein are captured by the distribution Eq. 1. This implicitly assumes that there is no feedback control from the output to the ligand input, i.e. no "sculpting" of the morphogen ligand profile. We revisit this point in the Discussion. Thus, given a distribution of the morphogen input, we address a *local, cell-autonomous* morphogenetic decoding that allows the cells to tune their reading dynamically.

We subject the *local, cellular* reading to an open-loop control on total (ligand bound plus unbound) surface availability of the signalling ψ and non-signalling ϕ receptors. In our analysis we consider a family of monotonic (increasing or decreasing in x) receptor profiles, which for convenience we take to be of the Hill form, i.e. either

$$\text{Monotonically increasing in } x : f_A(x) = A_0 + \frac{A_1 x^a}{A_2^a + x^a} \quad \text{or} \tag{8}$$

$$\text{Monotonically decreasing in } x : f_B(x) = B_0 + \frac{B_1}{1 + (x/B_2)^b} \tag{9}$$

The range of values for these parameters considered in the numerical analysis are listed in Table. I. Therefore, when considering $\psi(x)$ to be monotonically increasing in x, we parametrise it with f_A. It follows that in a one-branch channel, there are two possibilities: $\psi \in \{f_A, f_B\}$ while in a two-branch channel, there are a total of four possibilities: $(\psi, \phi) \in \{f_A, f_B\} \times \{f_A, f_B\}$. This allows us to simulate the "reading" step performed by the cells (see Fig. 1**b**).

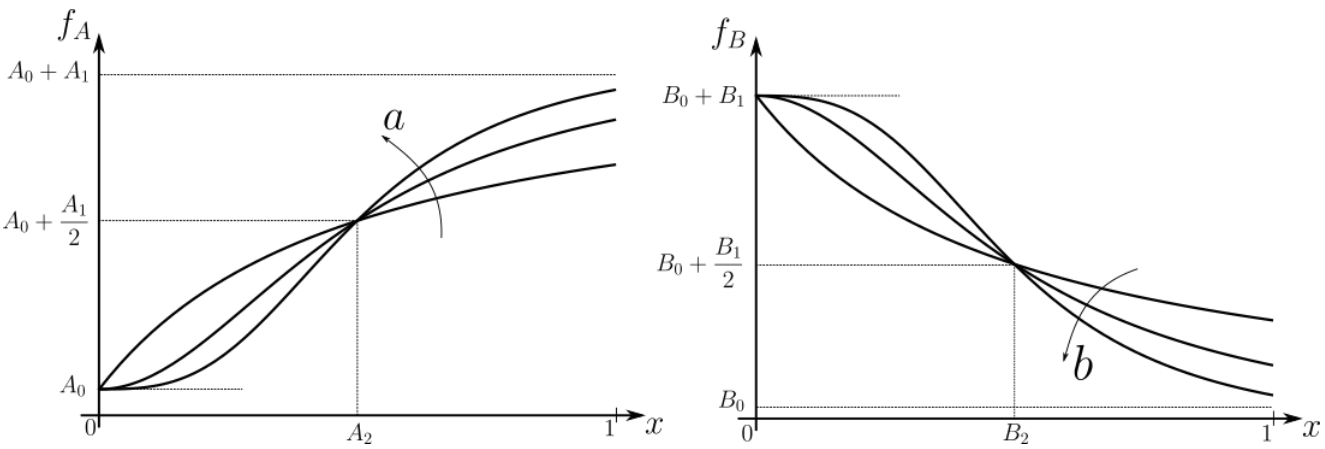

Figure 3. Family of receptor profiles f_A (monotonically increasing in x) and f_B (monotonically decreasing in x) with an interpretation of function parameters (Eq. 8-9).

Note that we are not fixing a receptor profile but taking it from a class of monotonic profiles (including a uniform profile), over which we vary to determine the optimal inference (see Section II C below). Monotonicity implicitly assumes a spatial correlation in the receptor concentrations – we return to this point in the Discussion.

Dynamics of processing in a single-tier channel. In a single tier channel, all processing is restricted to the cell surface. We represent the bound state of the signalling receptor as $R^{(1)}$ and that of the non-signalling receptor as $S^{(1)}$. The conjugated state is represented by $Q^{(1)}$. The CRN for such a system with one and two branches is shown in Fig. 4**a**. Rates associated with these reactions are listed in Table. I. The differential equations that describe the binding, unbinding, conjugation and degradation reactions of the receptors are given by

$$\partial_t R^{(1)} = r_b L(\psi(x) - R^{(1)}) - (r_u + r_d) R^{(1)} - \kappa_C R^{(1)} S^{(1)} + \kappa_S Q^{(1)} \tag{10}$$

$$\partial_t S^{(1)} = \kappa_b L(\phi(x) - S^{(1)}) - (\kappa_u + \kappa_d) S^{(1)} - \kappa_C R^{(1)} S^{(1)} + \kappa_S Q^{(1)} \tag{11}$$

$$\partial_t Q^{(1)} = \kappa_C R^{(1)} S^{(1)} - \kappa_S Q^{(1)} \tag{12}$$

The steady-state output θ, defined as the sum of all the ligand-bound signalling states, is given by $\theta = R^{(1)} + Q^{(1)}$. Note that to describe the 1-branch system, we simply set all rates κ to zero.

Dynamics of processing in a multi-tier channel. In a multi-tiered channel, the receptors go through additional steps of processing before generating an output. We represent the bound state of a receptor in k-th tier of the first branch as $R^{(k)}$, that of the second branch as $S^{(k)}$, and the conjugate species that forms in the last n_T-th tier as $Q^{(n_T)}$. The CRN for such a system with n_T tiers is shown in Fig. 4**b**. Rates associated with these reactions are listed in Table. I. The following differential equations describe the dynamics of this system.

$$\partial_t R^{(1)} = r_b L(\psi(x) - R^{(1)}) - (r_u + r_d + r_I)R^{(1)} + r_R R^{(2)} \tag{13}$$
$$\partial_t S^{(1)} = \kappa_b L(\phi(x) - S^{(1)}) - (\kappa_u + \kappa_d + \kappa_I)S^{(1)} + \kappa_R S^{(2)} \tag{14}$$
$$\vdots$$
$$\partial_t R^{(n_T)} = r_I R^{(n_T-1)} - (r_R + r_d)R^{(n_T)} - \kappa_C R^{(n_T)} S^{(n_T)} + \kappa_S Q^{(n_T)} \tag{15}$$
$$\partial_t S^{(n_T)} = \kappa_I S^{(n_T-1)} - (\kappa_R + \kappa_d)S^{(n_T)} - \kappa_C R^{(n_T)} S^{(n_T)} + \kappa_S Q^{(n_T)} \tag{16}$$
$$\partial_t Q^{(n_T)} = \kappa_C R^{(n_T)} S^{(n_T)} - \kappa_S Q^{(n_T)} \tag{17}$$

The output now becomes $\theta = w_{n_T} Q^{(n_T)} + \sum_{k=1}^{n_T} w_k R^{(k)}$ at steady state with w_k, such that $\sum_k w_k = 1$, representing the weight allotted to the tier (according to the mean residence time in the tier, for instance). For details regarding the setup of Eqs. 10-12 and 13-17 refer Appendix A.

These differential equations for single-tiered and multi-tiered systems are to be augmented by stochastic contributions from both extrinsic and intrinsic sources. Extrinsic noise is a consequence of stochasticity of the ligand concentration presented to the cell, $L \sim p(L|x)$, and enters the equations as a source term. On the other hand, intrinsic noise is a consequence of copy-number fluctuations in the CRNs that characterise the channel, and are treated using chemical master equations (CMEs).

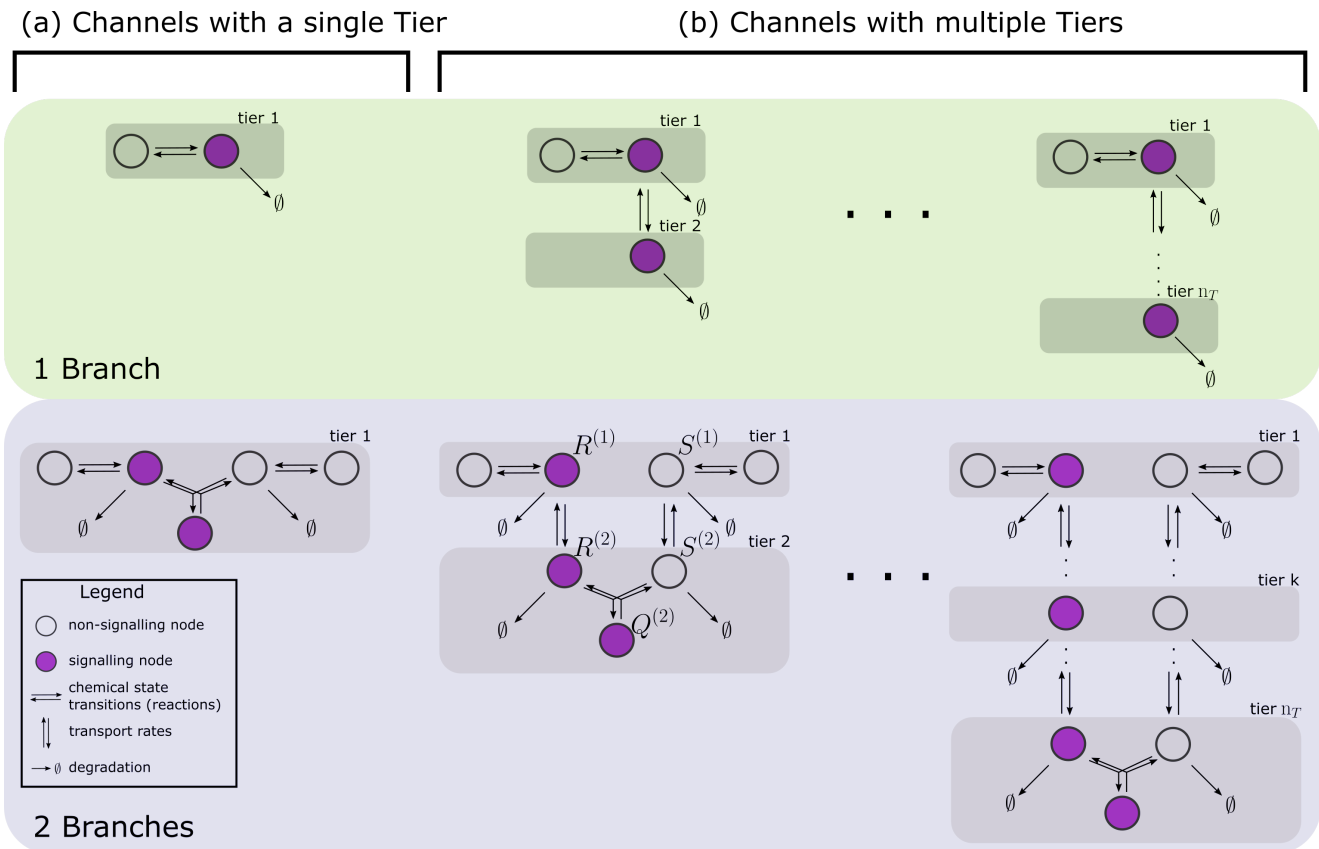

Figure 4. Examples of channel architectures with single and multiple tiers, and upto two branches. Signalling receptors in the bound state (colour purple) from each of the tiers contribute to the cellular output.

Feedback Control. We consider all rates in the CRN, except the ligand binding and unbinding rates, as potentially under feedback regulation. Any rate $r \in \{r_I, \kappa_I, \kappa_C, ...\}$ that is under feedback control actuated by

the node $R \in \{R^{(1)}, S^{(1)}, ...\}$ is modelled as

$$r_+ = r_0 \left(1 + \frac{\alpha R^n}{\gamma^{-n} + R^n}\right) \quad \text{if under positive feedback} \tag{18}$$

$$r_- = \frac{r_0}{1 + (\gamma R)^n} \quad \text{if under negative feedback} \tag{19}$$

with r_0 as the reference value of the rate in absence of feedback. The range of values for amplification α, feedback sensitivity γ and feedback strength n are listed in Table. I. Fig. 5 shows the different categories of possible feedback controls. We discuss the heuristics underlying the feedback controls in Appendix B.

C. Performance of the Channel Architectures

With the model in place, we address the **Objective** discussed previously, by studying the performance of different channel architectures, i.e. number of tiers and branches, and feedback topology. We define a vector $\vec{v}$ of the channel parameters related to chemical rates, receptor profiles and feedback (see Table I). For a given morphogen input distribution $p(L|x)$ and a channel architecture under consideration, the optimisation can be stated as

$$\bar{\sigma}_X^{\text{opt}} = \min_{\vec{v}} \bar{\sigma}_X(\vec{v}; p(L|x)) \tag{20}$$

and implemented by the following algorithm, the details of which are presented in Appendix C.

Optimisation scheme

1. Fix a morphogen input distribution for each position, $p(L|x)$ using Eq. 1
2. Define the channel architecture hierarchically, i.e. first declare the number of tiers and branches in the channel, and then choose a feedback topology (as in Fig. 5).
3. Optimise the average inference error Eq. 20 w.r.t. to the channel parameters $\vec{v}$ within the bounds provided in Table I. We use a gradient independent method viz. Pattern Search algorithm for this step (implemented in MATLAB). For every poll (iteration) of the Pattern Search, we calculate average inference error $\bar{\sigma}_X$ using the steady-state outputs of the equations corresponding to the CRN under optimisation i.e. Eqs. 10-17. The steady state solution is obtained analytically when possible or solved using ODE15s (MATLAB) algorithm.
4. Repeat Step 3 until all feedback topologies under consideration are exhausted.
5. Repeat Steps 2 & 3 until all channel architectures are scanned.

III. RESULTS

As discussed previously, cells of a developing tissue face both extrinsic as well as intrinsic sources of noise. We first look at the issue of extrinsic noise in the morphogen input (described by Eq. 1). The output is a deterministic function of the morphogen input and parameters of the channel i.e. receptor concentrations, feedback topology, rates and feedback parameters. The range of values considered for these parameters is listed in Table I. We apply the numerical analysis and the optimisation algorithm outlined in Section II to determine the design characteristics of "reading" (receptor profiles) and "processing" (tiers and feedback control) steps. Later, we check how channels, optimised in the reading and processing steps to deal with extrinsic noise, respond to intrinsic noise and what roles the elements of channel architecture play there. All the essential results are presented in this section and the reader may look up the appendices for further details.

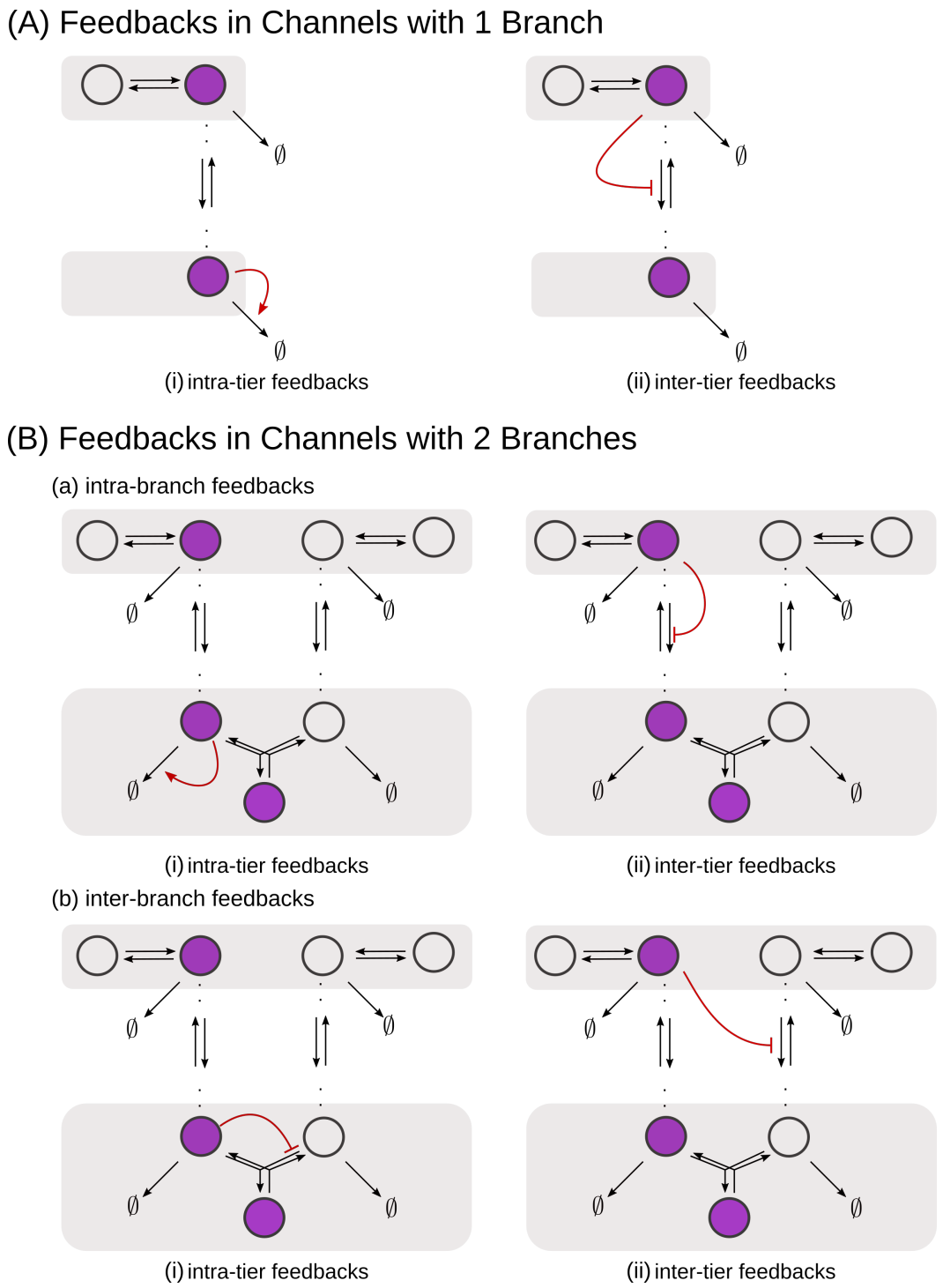

Figure 5. Schematic of several feedback types. **(A)** In a one-branch channel, feedbacks are considered on internalisation rates or degradation rates. **(B)** A second branch in the channel opens up the possibilities of (a) intra-branch and (b) inter-branch, (i) intra-tier and (ii) inter-tier feedbacks.

A. Branched architecture with multiple receptors provides accuracy and robustness to extrinsic noise

We begin with architectures comprising single-tiered channels with one and two branches. Such architectures are similar in design to the classic picture of ligand-receptor kinetics [47, 48], but also to the self-enhanced degradation models for robustness of morphogen gradients [19]. Before we proceed, it helps to recall a simple heuristic regarding signal discrimination. Appendix D Fig. 12 illustrates that precision in positional inference requires both that the output variance at a given position be small and that the mean output at two neighbouring positions be sufficiently different.

Let us first consider a *minimal* architecture of a one-tier one-branch channel without feedback control on any of the reaction rates. The output of this channel, here $R^{(1)}$, is a monotonic, saturating function of the input, with the surface receptor concentration setting the asymptote. As in Appendix E Fig. 16**a**, if the receptor concentrations decrease with mean ligand input, i.e. increases with distance from source (f_A in Fig. 3**a**), the outputs for different input ranges overlap significantly. On the other hand, if the receptor concentrations increase with mean input (f_B in Fig. 3**b**), the outputs overlap to a lesser degree (see Appendix E Fig. 16**b**). Thus within this minimal architecture, the inference error is optimised when the receptor concentrations increase with the mean input.

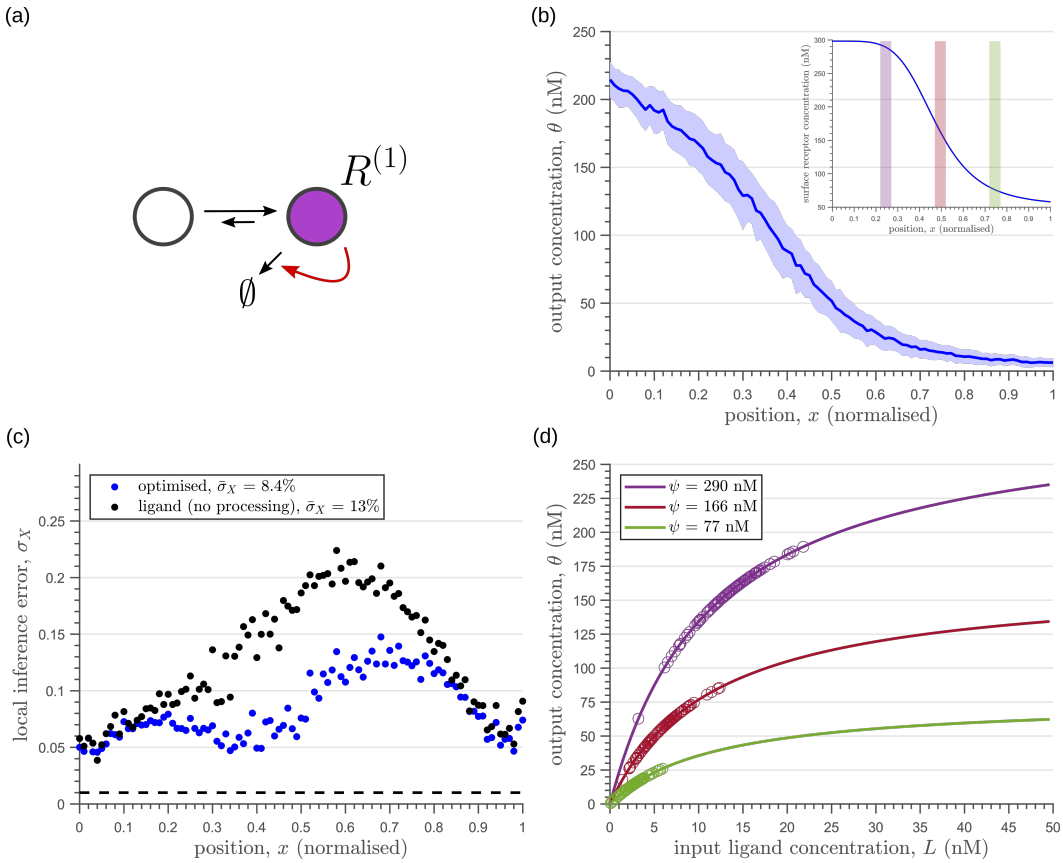

Figure 6. Characteristics of an optimised **(a)** one-tier one-branch channel. The optimised channel shows a moderately strong positive feedback on the degradation rate. **(b)** The optimal output is obtained when **(b, inset)** the signalling receptor profiles show an increase with mean ligand. **(c)** Consistent with the above, local inference errors show a reduction compared to the expected inference errors from ligand with no cellular processing. The minimum average inference error in this channel is $\bar{\sigma}_X \sim 8\%$. The dashed line corresponds to a local inference error of one cell's width $\sim 1/n_x$. However, **(d)** the input-output relations in this channel are restricted to monotonically increasing sigmoid functions saturating at only large values of input. The plots correspond to the receptor profiles at positions shaded with the same colour in (b, inset). The solid lines represent the input-output relation for the corresponding receptor combinations while the circles show the values of input-output pairs realised in the optimised channels. The optimised parameter values for the plots in (b-d) can be found in Table II under the column corresponding to $n_T = 1, n_B = 1, r_+ = r_d^{(1)}$.

Introducing a feedback in this one-tier one-branch architecture, either on receptor levels or degradation rate, only partially reduces the inference errors (Fig. 6**a,c**). This is because the surface receptor concentration ψ sets both the asymptote and the steepness of the input-output functions, resulting in a lack of clear separation between outputs at neighbouring positions. The receptor control introduces a competition between *robustness* of the output to input noise and *sensitivity* to systematic changes in the mean input (see Appendix D).

Including an additional *branch* in the channel architecture opens up several new possibilities of feedback controls. Further, concentration of non-signalling receptor ϕ provides an additional tuning variable. Now, as opposed to the one-tier one-branch case, an inter-branch feedback control (Fig. 7**a**) results in an input-output relation with a sharp rise followed by a saturation (Fig. 7**d**). By appropriately placing the receptors at spatial locations that receive different input, as shown by black arrow in Fig. 7**d**, one can cleanly separate out the outputs from neighbouring positions. For a detailed description see Appendix F. This mitigates the tension between *robustness* to input noise and *sensitivity* to systematic changes in the mean input to a considerable extent (see Appendix D Fig. 13).

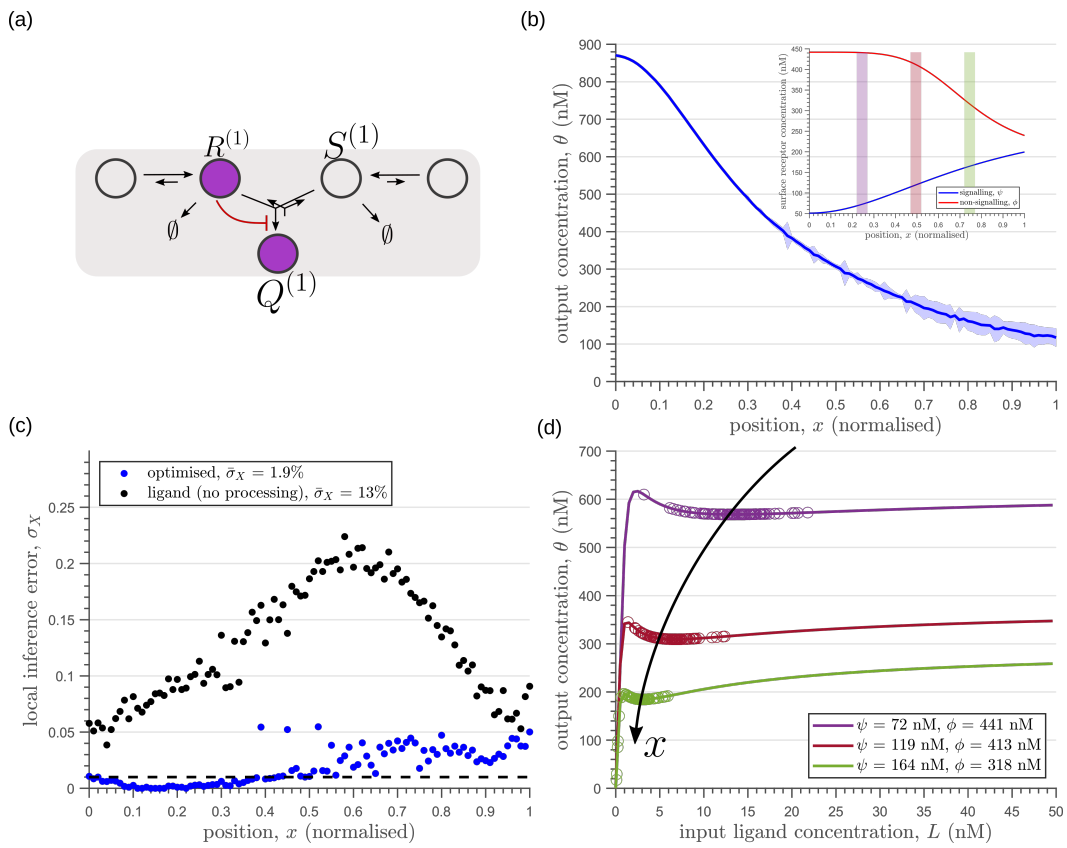

Figure 7. Results of optimisation of **(a)** one-tier two-branch channel. **(b)** The output profile (with standard error in shaded region) corresponding to the **(inset)** optimised signalling (blue) and non-signalling (red) receptor profiles. **(c)** The local inference error $\sigma_X(x)$ is reduced throughout the tissue, when compared to the expected inference errors from ligand with no processing. **(d)** Tuning of input-output relations through receptor concentrations reduces output variance and minimises overlaps in the outputs of neighbouring cell cohorts. The plots correspond to the receptor profiles at positions (in the direction of the black arrow) shaded with the same colour in (b, inset). The solid lines represent the input-output relation for the corresponding receptor combinations while the circles show the values of input-output pairs realised in the optimised channels. The optimised parameter values for the plots in (b-d) can be found in Table II under the column corresponding to $n_T = 1, n_B = 2, r_- = \kappa_C$.

B. Tiered architecture with compartmentalisation adds robustness to intrinsic noise

We next investigate the effects of addition of tiers (compartments) on the inference errors. Our optimisation shows there are two distinct optimised two-tier two-branch architectures with inter-branch feedback topologies that have comparable inference errors, Fig. 8. Both the receptor profiles and the input-output relations of these two optimised two-tier two-branch channels are qualitatively similar (Fig. 8**b-d,f-h**).

It would seem that addition of further tiers, i.e. more than two, would lead to improved inference. However, in both these optimised architectures, further addition leads only to a marginal reduction of inference errors (Appendix G Fig. 18) while invoking a cellular cost. Of course, extensions of our model that involve modification of the desired output could favour the addition of more tiers. For instance, additional tiers could facilitate signal amplification or improvement in *robustness* to input noise through an increase in signal-to-noise ratio (SNR) [49]. Further, by making the output θ a multi-variate function of the tier index (compartment identity) one can multitask the various cellular outcomes (as in Ras/MAPK signalling [50] or with GPCR compartmentalisation [35]).

So far we have only considered noise due to fluctuations in the morphogen profile, i.e. extrinsic noise. Given that we are considering a distributed channel, intrinsic noise due to low copy numbers of the reacting species in the CRN will have a significant influence on the inference. As discussed in Section II and Appendix C, we solve the stochastic chemical master equations (CMEs) to compute the output distributions and the positional inference. It is here that we find that the addition of tiers contribute significantly to reducing inference errors. A comparison of the one-tier two-branch and two-tier two-branch channel architectures (Fig. 9**a,b**) optimised for extrinsic noise, shows that in the presence of intrinsic noise, additional tiers lead to significantly lower inference errors (Fig. 9**c**). The large inference errors seen in the one-tier one-branch channel in the presence of intrinsic noise, can be traced to the instabilities of steady-state trajectories of the two signalling species $R^{(1)}$ and $Q^{(1)}$ driven by the non-linear feedback (Fig. 9**d-f**). This effect is more prominent for larger values of ligand concentrations, i.e. closer to the source at $x = 0$. On the other hand, we find that in the two-tier two-branch architecture (Fig. 9**g-i**), the fluctuations in the signalling species are more tempered, the inter-branch feedback leads to a mutual damping of the fluctuations of the signalling species from the two branches. Details of this heuristic argument appear in Appendix H.

In summary, we find that the nature of the channel architectures play a significant role in robustness of morphogenetic decoding to both extrinsic and intrinsic sources of noise. Of the three elements to the channel architecture - branches, tiers and feedback control, we find that a branched architecture can significantly reduce inference errors by employing an inter-branch feedback control and a control on its local receptor concentrations. For this, the receptor concentration profiles required to minimise inference errors are such that the concentration of signalling (non-signalling) receptor should decrease (increase) with mean morphogen input. Crucially, in the absence of feedback, performance of the channel diminishes and the optimised receptor profiles are *both* decreasing functions of x (Appendix K Fig. 24). Further, we show in Appendix L Fig. 25 that having uniform profiles for the signalling and non-signalling receptors, with or without uncorrelated noise, fares poorly in terms of inference capability. This provides *a posteriori* justification for the monotonicity in receptor profiles. Addition of tiers can help in further bringing down inference errors due to extrinsic noise, but with diminishing returns. An additional tier, however, does provide a buffering role for feedback when dealing with intrinsic noise. We note that these qualitative conclusions remain unaltered for different morphogen input characteristics, i.e. input noise and morphogen decay lengths (see Appendix J).

C. Asymmetry in branched architecture: promiscuity of non-signalling receptors

Before comparing the theoretical results with experiments, we comment on the implications for the cellular control of the signalling ψ and non-signalling ϕ receptors. In the two-branched architecture, the symmetry between the signalling and non-signalling receptors is broken by the inter-branch feedback and the definition of output θ, taken to be a function only of the signalling states $R^{(k)}$ and $Q^{(k)}$ (Section II, purple nodes in Fig. 7**a** and Fig. 8**a,e**). What are the phenotypic implications of this asymmetry? In Appendix I Fig. 21, we plot the contours of average inference errors $\bar{\sigma}_X$ in the $\psi - \phi$ plane around the optimal point. The difference in the magnitudes of the eigenvalues of the Hessian at this point immediately describe rigid and sloppy directions [51] along the ψ and ϕ axes, respectively. This implies that while the signalling receptor is under tight cellular control, the control on the non-signalling receptor is allowed to be sloppy. A similar feature is observed in the contour plots for the robustness

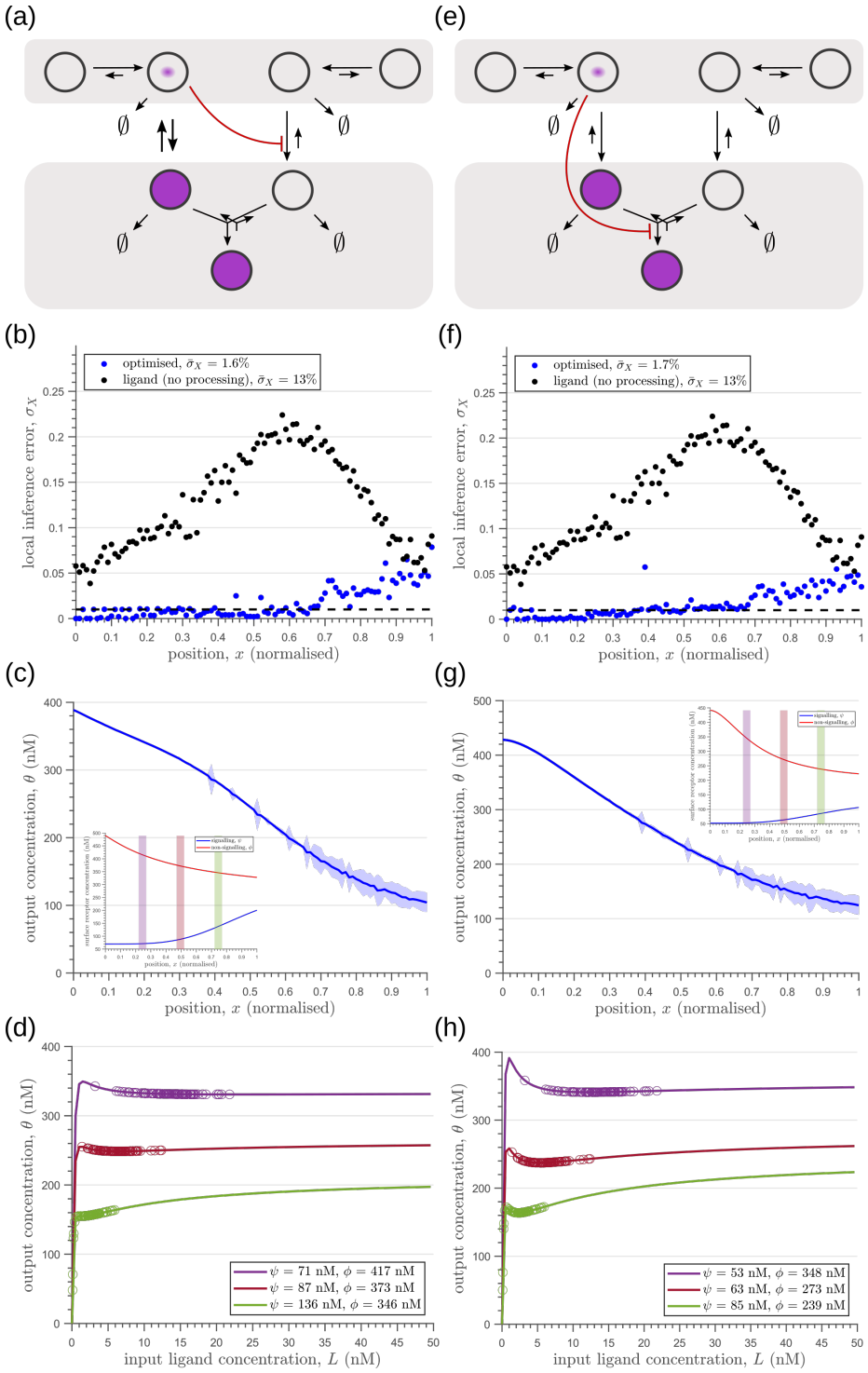

Figure 8. Results of optimisation of **(a,e)** two-tier two-branch channels. These two architectures with inter-branch feedbacks perform equally well. **(b,f)** As compared to a case with no processing of ligand prior to inference (black dots), local inference errors in both the channels (blue dots) are low throughout the tissue (with average inference errors $\sim 1.6\%$ and $\sim 1.7\%$). However, local inference errors always tend to rise away from the source due to lower ligand concentrations. The dashed line corresponds to a local inference error of one cell's width $\sim 1/n_x$. **(c,g)** The output profile (with standard error in shaded region) corresponding to the **(inset)** optimised signalling (blue) and non-signalling (red) receptor profiles. **(d,h)** Tuning of input-output relations through receptor concentrations. The plots correspond to the receptor profiles at positions shaded with the same colour in (c,g insets). The solid lines represent the input-output relation for the corresponding receptor combinations while the circles show the values of input-output pairs realised in the optimised channels. The optimised parameter values for the plots in (b-d,f-h) can be found in Table II under the column corresponding to $n_T = 2, n_B = 2, r_- = \kappa_I$ and $n_T = 2, n_B = 2, r_- = \kappa_C$, respectively.

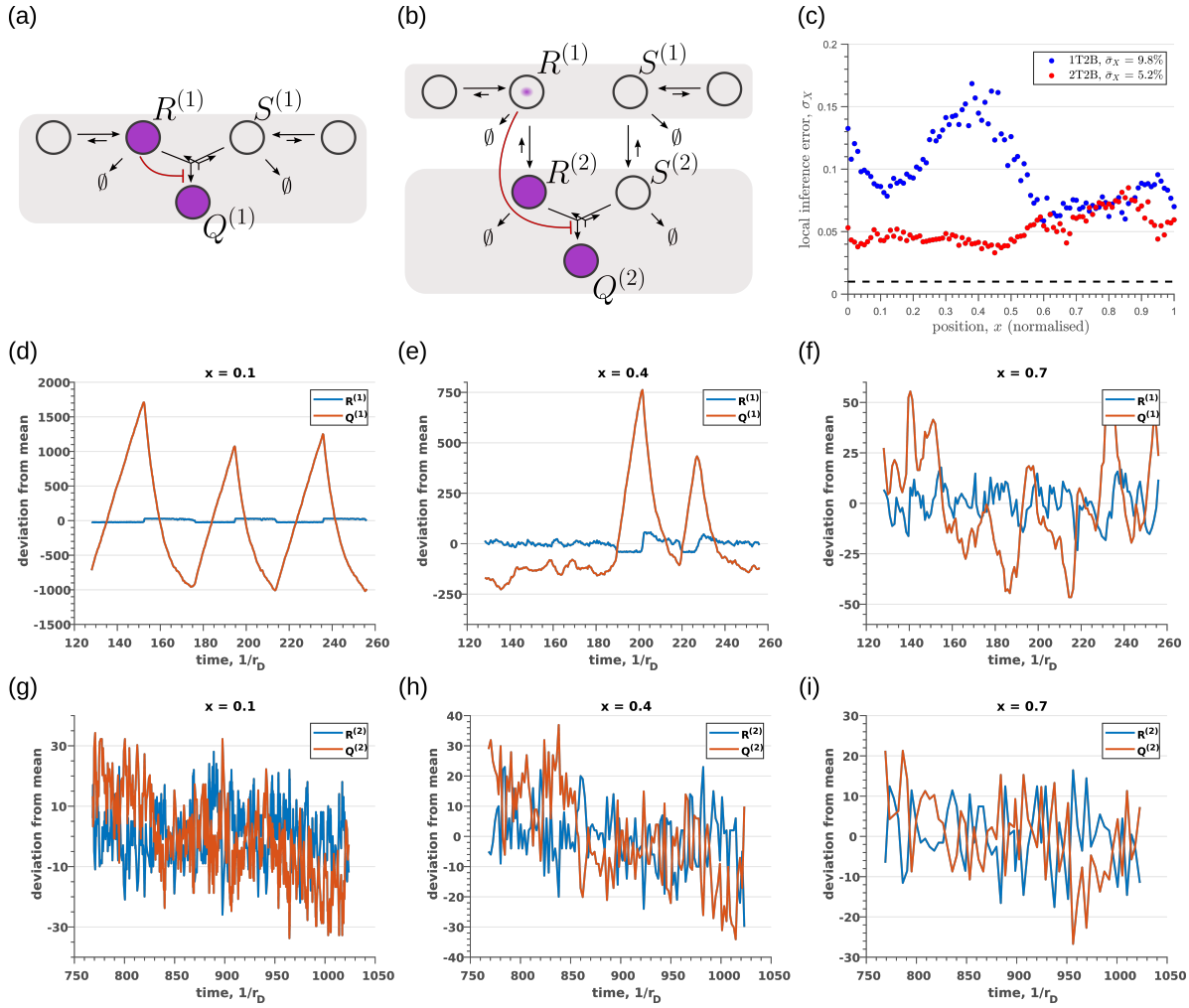

Figure 9. Robustness to intrinsic noise in **(a)** one-tier two-branch (1T2B) channel and **(b)** two-tier two-branch (2T2B) channel architectures optimised for extrinsic noise alone. **(c)** A comparison of local inference errors due to intrinsic noise shows consistently better performance in the case of a two-tier two-branch channel (red dots). **(d-f)** Sample steady-state trajectories of the signalling species $R^{(1)}$ (blue) and $Q^{(1)}$ (red) of a one-tier two-branch channel at positions $x = 0.1, 0.4, 0.7$, respectively. **(g-i)** Sample steady-state trajectories of the signalling species $R^{(2)}$ (blue) and $Q^{(2)}$ (red) of a two-tier two-branch channel at positions $x = 0.1, 0.4, 0.7$, respectively. The optimised parameter values for the plots in (c,d-f,g-i) can be found in Table II under the column corresponding to $n_T = 1, n_B = 2, r_- = \kappa_C$ and $n_T = 2, n_B = 2, r_- = \kappa_C$, respectively.

measure χ (defined as the ratio of coefficients of variation in the output to that in the input). Appendix D Fig. 14 shows that for any given input distribution, reduction in output variance requires a stricter control on ψ while the control on ϕ can be lax.

This sloppiness in the non-signalling receptor would manifest at a phenomenological level in the context of multiple morphogen inputs as in the case of *Drosophila* imaginal disc [3]. Participation of the same non-signalling receptor in the different signalling networks would imply its promiscuous interactions with all ligands. The signalling receptors, therefore, are *specific* for the various ligands while the non-signalling receptor, being promiscuous, is *non-specific*. This, as we see below, is the case with the Heparan sulfate proteoglycans (HSPGs) such as Dally and Dally-like protein (Dlp) that participate in the Wingless (Wg) and Decapentaplegic (Dpp) signalling networks [52, 53].

D. Experimental verification in the *Drosophila* Wg signalling system

The phenomenology of the morphogen reading and processing of Wg in the wing imaginal disc of *Drosophila melanogaster* [39] suggests a one-to-one mapping to the two-tier two-branch channel defined above, thus providing an ideal experimental system for a realisation of these ideas (Fig. 10**a,b**).

Wg is secreted by a line of cells (1-3 cells) at the dorso-ventral boundary and forms a concentration gradient across the receiving cells [54]. Receiving cells closer to the production domain show higher Wg signalling while those further away have lower Wg signalling [54]. Several cell autonomous factors influence reading and processing of the morphogen Wg in the receiving cells. Binding of Wg to its signalling receptor, Frizzled-2, DFz2, initiates signal transduction pathway and nuclear translocation of β-catenin which further results in activation of Wg target genes (reviewed in [55]). In addition to the signalling receptor, binding receptors such as Heparin Sulphate Proteoglycans (HSPGs) – Dally and Dlp also contribute to Wg signalling [30, 56]. Further, the two receptors follow distinct endocytic pathways [39]: while, DFz2 enters cells via the Clathrin Mediated Endocytic pathway (CME), Wg also enters cells independent of DFz2, possibly by binding to HSPGs, through CLIC/GEEC (CG) endocytic pathway. The two types of vesicles, containing Wg bound to different receptors, merge in common early endosomes [39]. However, only DFz2 receptors in their Wg bound state, both at the cell surface and early endosomes, are capable of generating a downstream signal leading to positional inference through a transcriptional readout [57]. This phenomenology is faithfully recapitulated in our two-tier two-branch channel architecture (Fig. 10**b**) in which DFz2 and HSPG receptors play the role of the two branches.

Since an experimental measurement of positional inference error poses difficulties, we measure the cell-to-cell variation in the signalling output for a given position x as a proxy for inference error (Appendix D Fig. 14). Larger the variation, higher is the inference error. This is calculated as coefficient of variation (CV, Appendix M) in the output across cells in the y-direction (Fig. 10**c**).

Let us first discuss the results from the theoretical analysis. The optimised two-tier two-branch channel (Fig. 10**b**) shows that the magnitude and the fluctuations in the coefficients of variation are small, with a slight increase with position (blue, Fig. 10**f**). This is consistent with the low inference error associated with the optimised channel (Fig. 8**e**). Upon perturbing this channel via removal of the non-signalling branch, the magnitude and fluctuations in the signalling output variation increases significantly (orange, Fig. 10**e**). This qualitative feature of the coefficient of variation in the optimised two -tier two-branch channel is replicated in the Wg measurements of wild type cells.

In the experiments, we first established the method by determining the CV of a uniformly distributed signal, CAAX GFP (expressed using ubiquitin promoter), and observed that the CV of CAAX-GFP is relatively uniform in x, the distance from Wg producing cells (Fig. 10**d**). In order to study the steady state distribution of Wg within a cell and the endosomes it occupies, we performed a long endocytic pulse (1 hour) with fluorescently labelled antibody against Wg ([39], Prabhakara et al., in preparation). Following this, we estimated the CV of the Wg endocytic profile as a function of x (Fig. 10**f**, and Appendix M Fig. 26).

We assessed the CV of endocytosed Wg under two conditions: one, where the endocytic pulse of Wg is captured by the two branches and two tiers (control condition), and another, where we disengage one of the tiers by inhibiting the second endocytic pathway using a genetically expressed dominant negative mutant of Garz, a key player in the CG endocytic pathway [58]. This perturbation has little or no effect on the functioning of the CME or the levels of the surface receptors that are responsible for Wg endocytosis ([39]; Prabhakara et al in preparation). As in the theory (Fig. 10**e**), CV in the control shows a slight increase with position (Fig. 10**f**) with fluctuations about the mean profile being small. In the perturbed condition, with the CG endocytic pathway disengaged, we find the CV shows a steeper increase with x and has larger fluctuations about the mean profile.

In principle, the coefficient of variation of the output is affected by all the microscopic stochastic processes that intersect with Wg signalling network in the wing imaginal disc and in the ligand input. Therefore, one has to be careful about interpreting the changes in the coefficient of variation of the output, based on the such perturbation experiments. Notwithstanding, this qualitative agreement between theory and experiment is encouraging.

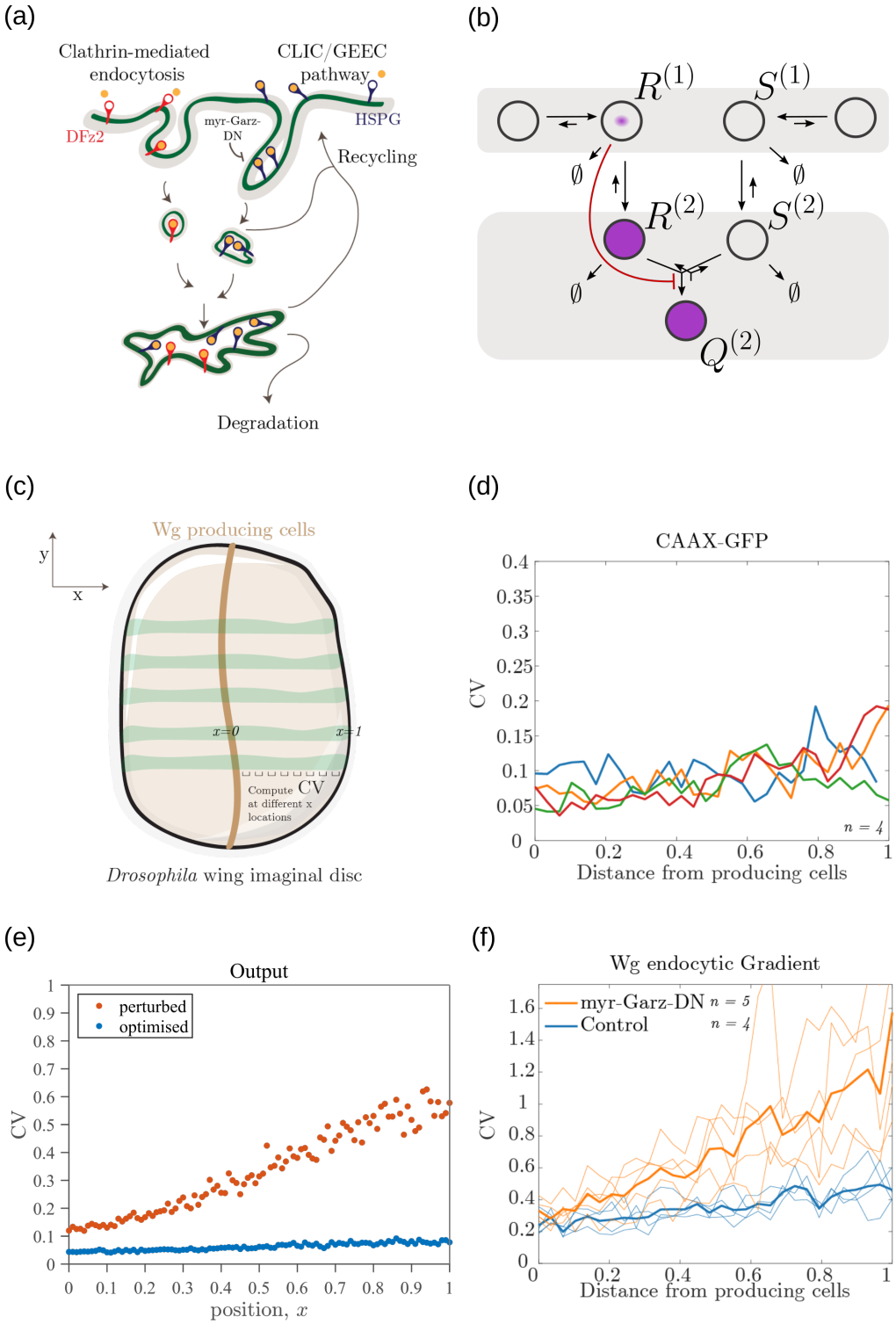

Figure 10. Comparison of theoretical results with experimental observations on Wg signalling system in *Drosophila* wing imaginal disc. **(a)** Schematic of the cellular processes involved in Wg signalling, showing the two endocytic routes for the receptors (see text for further description). **(b)** Two-tier two-branch channel architecture corresponding to the Wg signalling system. **(c)** Schematic describing the XY view of wing disc. The vertical brown stripe marks the Wg producing cells. Horizontal green stripes mark the regions in wing disc used for analysis. See methods for more information. **(d)** Coefficient of variation (CV) of CAAX-GFP intensity profiles, expressed in wing discs, as a function of (normalized) distance from producing cells (n=4). **(e)** Coefficient of variation in the output of the optimised two-tier two-branch channel (blue), and upon perturbation (orange) via removal of the non-signalling branch, implemented by setting all rates in the non-signalling branch κ to zero. The optimised parameter values for the plot can be found in Table II under the column corresponding to $n_T = 2, n_B = 2, r_- = \kappa_C$. **(f)** CV of intensity profiles of endocytosed Wg in control wing discs (C5GAL4Xw1118; blue; n= 4) and discs wherein CLIC/GEEC endocytic pathway is removed using UAS-myr-garz-DN (C5GAL4XUAS-myr-garz-DN; orange; n=5).

IV. DISCUSSION

In this paper, we have posed the problem of spatial patterning of cell fates in a developing tissue as a *local, cell autonomous* morphogenetic decoding that ensures precise inference of position, that is robust to extrinsic and intrinsic noise. We treat the cells as inference channels capable of reading and processing the morphogen input. We describe the architecture of the inference channels in terms of three elements: branches (number of receptor types), tiers (number of compartments) and feedbacks. We ask for properties of the inference channel architectures that allow for precision and robustness in the task of morphogenetic decoding.

We show that having a combination of a specific signalling receptor and a promiscuous non-signalling receptor, and cellular compartmentalisation, can significantly improve the performance of cells in their positional decoding. Branched architectures with multiple receptors, in tandem with inter-branch feedback controls, provide robustness to extrinsic noise. Having a multi-tier architecture via cellular compartmentalisation provides robustness against intrinsic noise. This improvement in performance is contingent on having opposing profiles of the two receptor types.

Note that in our study, we have ignored cellular costs due to compartmentalisation, additional receptors and implementation of feedback controls, and thus possible trade-offs between cellular economy and precision in inference.

We next compare our results with experimental observations from Wg morphogen system of *Drosophila* wing imaginal disc. We first show that Wg signalling in the experimental system is equivalent to a two-tier two-branch channel. In the experiments, we use signal-to-noise ratio (SNR) of the output as a proxy for robustness of inference. Perturbation of the architecture, i.e. removal of the non-signalling branch, results in reduction of SNR. In a forthcoming manuscript, we will provide a detailed verification of the predicted opposing receptor profiles.

In our theoretical analysis, the difference between the signalling and the non-signalling receptors shows up in the extent to which they influence inference errors in the neighbourhood of the optimum (Section III C). We see that slight changes in the signalling receptor away from the optimum lead to a sharp increase in inference error while similar changes in the non-signalling receptor do not affect the inference errors significantly. This gives rise to the notion of stiff and sloppy directions of control - with non-signalling receptor placed under sloppy control. In a context with multiple morphogen ligands setting up the different coordinate axes (e.g. Wg, Dpp and Hh in imaginal discs [52, 59]), the non-specific receptor can potentially facilitate cross-talks between them. A sloppy control on non-specific receptor would allow for accommodation of robustness in the outcomes of the different morphogens. This could potentially be tested in experiments.

We end our discussion with a list of tasks that we would like to take up in the future. First, the information processing framework established here is very general. Obvious extensions of our models, such as adding more branches, tiers and chemical states, will not lead to any qualitatively new features. However, one may alter the objective function – for instance, in the case of short range morphogens like Nodal [45], only the positions of certain *regions* (closer to the morphogen source) or *cell fate boundaries* need to be specified with any precision.

Second, our theoretical result that the optimised surface receptor profiles are either monotonically increasing or decreasing from the morphogen source, suggests that the surface receptor concentrations are spatially correlated across cells. Such correlations could have a mechanochemical basis, either via cell surface tension that could in turn affect internalisation rates [60] or inter-cellular communication through cell junction proteins [61] or from adaptive feedback mechanisms between the output and receptor concentrations [62]. We emphasize that in the current optimisation scheme, we allow the receptor concentrations to vary over the space of all monotonically increasing, decreasing or flat profiles, and do not encode the positional information in the receptor profiles.

Finally, as mentioned in Section II, we have considered the morphogen ligand as an *external input* to the receiving cells, outside the cellular information processing channel. There is no feedback from the output to the receptors and thus no “sculpting" of the morphogen ligand profile. Morphogen ligand profiles (e.g. Dpp [53]) are set by the dynamics of morphogen production at the source, diffusion via transcytosis and luminal transport, and degradation via internalisation. These cellular processes are common to both the reading and processing modules in our channel architecture. This would suggest a dynamical coupling and feedback between reading and ligand internalisation, which naturally introduces closed-loop controls on the surface receptors and a concomitant sculpting of the morphogen profile.

ACKNOWLEDGEMENTS

We thank Thomas Lecuit for insights during the course of investigation. We thank past and present members of the Simons Centre, especially Alkesh Yadav, Amit Kumar, Archishman Raju, Kabir Husain and Sandeep Krishna, for critical inputs. We acknowledge support from the Department of Atomic Energy (India), under project no. RTI4006, and the Simons Foundation (Grant No. 287975). MR and SM acknowledge DST (India) for JC Bose Fellowships. SM acknowledges a Margadarshi Fellowship of DBT-Wellcome Trust India alliance (IA/M/15/1/502018).

[1] G. Tkačik and T. Gregor, Development **148** (2021).
[2] L. Wolpert, Current topics in developmental biology **117**, 597 (2016).
[3] T. Tabata and Y. Takei, Development **131**, 703 (2004).
[4] J. Briscoe and S. Small, Development **142**, 3996 (2015).
[5] B. Houchmandzadeh, E. Wieschaus, and S. Leibler, Nature **415**, 798 (2002).
[6] T. Gregor, D. W. Tank, E. F. Wieschaus, and W. Bialek, Cell **130**, 153 (2007).
[7] A. Kicheva, P. Pantazis, T. Bollenbach, Y. Kalaidzidis, T. Bittig, F. Julicher, and M. González-Gaitán, Science **315**, 521 (2007).
[8] T. Bollenbach, P. Pantazis, A. Kicheva, C. Bökel, M. González-Gaitán, and F. Jülicher, Development **135** (2008).
[9] M. Zagorski, Y. Tabata, N. Brandenberg, M. P. Lutolf, G. Tkačik, T. Bollenbach, J. Briscoe, and A. Kicheva, Science **356**, 1379 (2017).
[10] T. Gregor, E. F. Wieschaus, A. P. McGregor, W. Bialek, and D. W. Tank, Cell **130**, 141 (2007).
[11] J. O. Dubuis, G. Tkačik, E. F. Wieschaus, T. Gregor, and W. Bialek, Proceedings of the National Academy of Sciences **110**, 16301 (2013).
[12] M. D. Petkova, G. Tkačik, W. Bialek, E. F. Wieschaus, and T. Gregor, Cell **176**, 844 (2019).
[13] M. Kerszberg and L. Wolpert, Cell **130**, 205 (2007).
[14] M. Kerszberg, Current opinion in genetics & development **14**, 440 (2004).
[15] J. Jaeger, S. Surkova, M. Blagov, H. Janssens, D. Kosman, K. N. Kozlov, E. Myasnikova, C. E. Vanario-Alonso, M. Samsonova, D. H. Sharp, et al., Nature **430**, 368 (2004).
[16] N. Barkai and B.-Z. Shilo, Cold Spring Harbor perspectives in biology **1**, a001990 (2009).
[17] A. D. Lander, W.-C. Lo, Q. Nie, and F. Y. Wan, Cold Spring Harbor perspectives in biology **1**, a002022 (2009).
[18] A. Eldar, R. Dorfman, D. Weiss, H. Ashe, B.-Z. Shilo, and N. Barkai, Nature **419**, 304 (2002).
[19] A. Eldar, D. Rosin, B.-Z. Shilo, and N. Barkai, Developmental cell **5**, 635 (2003).
[20] P. McHale, W.-J. Rappel, and H. Levine, Physical biology **3**, 107 (2006).
[21] S. Bergmann, O. Sandler, H. Sberro, S. Shnider, E. Schejter, B.-Z. Shilo, and N. Barkai, PLoS biology **5**, e46 (2007).
[22] T. Bollenbach, K. Kruse, P. Pantazis, M. González-Gaitán, and F. Jülicher, Physical Review E **75**, 011901 (2007).
[23] K. W. Rogers and A. F. Schier, Annual review of cell and developmental biology **27**, 377 (2011).
[24] T. D. Mueller and J. Nickel, FEBS letters **586**, 1846 (2012).
[25] X. Jiang and F. Cong, Trends in biochemical sciences **41**, 773 (2016).
[26] B. D'souza, A. Miyamoto, and G. Weinmaster, Oncogene **27**, 5148 (2008).
[27] Y. Chen and A. F. Schier, Current Biology **12**, 2124 (2002).
[28] S. Sick, S. Reinker, J. Timmer, and T. Schlake, Science **314**, 1447 (2006).
[29] L. Marjoram and C. Wright, Development **138**, 475 (2011).
[30] G.-H. Baeg, X. Lin, N. Khare, S. Baumgartner, and N. Perrimon, Development **128**, 87 (2001).
[31] G.-H. Baeg, E. M. Selva, R. M. Goodman, R. Dasgupta, and N. Perrimon, Developmental biology **276**, 89 (2004).
[32] D. Yan and X. Lin, Cold Spring Harbor perspectives in biology **1**, a002493 (2009).
[33] C. Bökel and M. Brand, Cold Spring Harbor Perspectives in Biology **6**, a017020 (2014).
[34] P. P. Di Fiore and M. von Zastrow, Cold Spring Harbor perspectives in biology **6**, a016865 (2014).
[35] A. M. Ellisdon and M. L. Halls, Biochemical Society Transactions **44**, 562 (2016).
[36] J. Omerovic, A. J. Laude, and I. A. Prior, Cellular and molecular life sciences **64**, 2575 (2007).
[37] J. Omerovic and I. A. Prior, The FEBS journal **276**, 1817 (2009).
[38] B.-Z. Shilo and E. D. Schejter, The EMBO journal **30**, 3516 (2011).
[39] A. Hemalatha, C. Prabhakara, and S. Mayor, Proceedings of the National Academy of Sciences **113**, E6993 (2016).
[40] D. Hartich, A. C. Barato, and U. Seifert, Journal of Statistical Mechanics: Theory and Experiment **2014**, P02016 (2014).
[41] I. Averbukh, A. Gavish, B.-Z. Shilo, and N. Barkai, Current Opinion in Systems Biology **1**, 69 (2017).
[42] S. E. Harvey, S. Lahiri, and S. Ganguli, arXiv preprint arXiv:2002.10567 (2020).

[43] D. J. MacKay and D. J. Mac Kay, Information theory, inference and learning algorithms (Cambridge university press, 2003).
[44] G. Tkačik, J. O. Dubuis, M. D. Petkova, and T. Gregor, Genetics **199**, 39 (2015).
[45] L. Liu, A. Nemashkalo, L. Rezende, J. Y. Jung, S. Chhabra, M. C. Guerra, I. Heemskerk, and A. Warmflash, Nature Communications **13**, 1 (2022).
[46] Y. Zhu, Y. Qiu, W. Chen, Q. Nie, and A. D. Lander, Developmental cell **53**, 724 (2020).
[47] D. A. Lauffenburger and J. J. Linderman, Receptors: models for binding, trafficking, and signaling (Oxford University Press on Demand, 1996).
[48] B. Alberts, A. Johnson, J. Lewis, D. Morgan, M. Raff, K. Roberts, P. Walter, J. Wilson, and T. Hunt, Molecular biology of the cell (WW Norton & Company, 2017).
[49] T. Stoeger, N. Battich, and L. Pelkmans, Cell **164**, 1151 (2016).
[50] N. Fehrenbacher, D. Bar-Sagi, and M. Philips, Molecular oncology **3**, 297 (2009).
[51] M. K. Transtrum, B. B. Machta, K. S. Brown, B. C. Daniels, C. R. Myers, and J. P. Sethna, J. Chem. Phys. **143**, 010901 (2015).
[52] X. Lin and N. Perrimon, Matrix biology **19**, 303 (2000).
[53] M. Romanova-Michaelides, Z. Hadjivasiliou, D. Aguilar-Hidalgo, D. Basagiannis, C. Seum, M. Dubois, F. Jülicher, and M. Gonzalez-Gaitan, Nature , 1 (2021).
[54] C. J. Neumann and S. M. Cohen, Development **124**, 871 (1997).
[55] H. Clevers and R. Nusse, Cell **149**, 1192 (2012).
[56] X. Franch-Marro, O. Marchand, E. Piddini, S. Ricardo, C. Alexandre, and J.-P. Vincent, Development **132**, 659 (2005).
[57] M. Tsuda, K. Kamimura, H. Nakato, M. Archer, W. Staatz, B. Fox, M. Humphrey, S. Olson, T. Futch, V. Kaluza, et al., Nature **400**, 276 (1999).
[58] G. D. Gupta, S. MG, S. Kumari, R. Lakshminarayan, G. Dey, and S. Mayor, PloS one **4**, e6768 (2009).
[59] X. Lin, Development **131**, 6009 (2004).
[60] J. J. Thottacherry, A. J. Kosmalska, A. Kumar, A. S. Vishen, A. Elosegui-Artola, S. Pradhan, S. Sharma, P. P. Singh, M. C. Guadamillas, N. Chaudhary, et al., Nature communications **9**, 1 (2018).
[61] M. A. Garcia, W. J. Nelson, and N. Chavez, Cold Spring Harbor perspectives in biology **10**, a029181 (2018).
[62] N. Barkai and S. Leibler, Nature **387**, 913 (1997).
[63] T. Jeeves and R. Hooke, Journal of the ACM **8**, 212 (1961).
[64] W. Sandmann, in Proceedings of the 2009 Winter Simulation Conference (WSC) (IEEE, 2009) pp. 1104–1112.
[65] F. Port, H.-M. Chen, T. Lee, and S. L. Bullock, Proceedings of the National Academy of Sciences **111**, E2967 (2014).
[66] N. A. Dye, M. Popović, S. Spannl, R. Etournay, D. Kainmüller, S. Ghosh, E. W. Myers, F. Jülicher, and S. Eaton, Development **144**, 4406 (2017).

Appendix A: Setting up the dynamical equations

The cellular processes involved in a general two-branch channel architecture, described in Section II B and Fig. 4, with any number of tiers n_T are: production of receptors, binding-unbinding of ligand with the receptors, intracellular transport between cellular compartments, conjugation and splitting in the final tier, and degradation of the chemical species involved. The mass action kinetics for these cellular processes are written as the following set of first-order ordinary differential equations (ODEs):

$$\begin{aligned}
\partial_t R_0^{(1)} &= r_p - (r_b L + r_d^{(1)}) R_0^{(1)} + r_u R_1^{(1)} \\
\partial_t R_1^{(1)} &= r_b L R_0^{(1)} - (r_u + r_d^{(1)} + r_I^{(1)}) R_1^{(1)} + r_R^{(1)} R_1^{(2)} \\
\partial_t S_0^{(1)} &= \kappa_p - (\kappa_b L + \kappa_d^{(1)}) S_0^{(1)} + \kappa_u S_1^{(1)} \\
\partial_t S_1^{(1)} &= \kappa_b L S_0^{(1)} - (\kappa_u + \kappa_d^{(1)} + \kappa_I^{(1)}) S_1^{(1)} + \kappa_R^{(1)} S_1^{(2)} \\
\partial_t R_1^{(2)} &= r_I^{(1)} R_1^{(1)} - (r_R^{(1)} + r_d^{(2)} + r_I^{(2)}) R_1^{(2)} + r_R^{(2)} R^{(3)} \\
\partial_t S_1^{(2)} &= \kappa_I^{(1)} S_1^{(1)} - (\kappa_R^{(1)} + \kappa_d^{(2)} + \kappa_I^{(2)}) S_1^{(2)} - \kappa_R^{(2)} S^{(3)} \\
&\;\;\vdots \\
\partial_t R_1^{(n_T)} &= r_I^{(n_T-1)} R_1^{(n_T-1)} - (r_R^{(n_T-1)} + r_d^{(n_T)}) R_1^{(n_T)} - \kappa_C R_1^{(n_T)} S_1^{(n_T)} + \kappa_S Q^{(n_T)} \\
\partial_t S_1^{(n_T)} &= \kappa_I^{(n_T-1)} S_1^{(n_T-1)} - (\kappa_R^{(n_T-1)} + \kappa_d^{(n_T)}) S_1^{(n_T)} - \kappa_C R_1^{(n_T)} S_1^{(n_T)} + \kappa_S Q^{(n_T)} \\
\partial_t Q^{(n_T)} &= \kappa_C R_1^{(n_T)} S_1^{(n_T)} - \kappa_S Q^{(n_T)}
\end{aligned} \tag{A1}$$

$R_j^{(k)}$ denotes species of the first branch, associated with the signalling receptor, in tier k and in bound ($j = 1$) or unbound ($j = 0$) states. Likewise $S_j^{(k)}$ denotes the same for the non-signalling receptor. $Q^{(n_T)}$ denotes the conjugated species in the final tier. Chemical rates related to the first branch are denoted by r while those in the second branch are denoted by κ. The processes of production, binding, unbinding, internalisation, recycling, conjugation, splitting and degradation are represented by the subscripts p, b, u, I, R, C, S, d, respectively (Table I). The superscript on degradation rate indicates the tier index, while the superscript over internalisation and recycling rates stands for the tier index of the species internalised by the pair of reactions.

With open-loop control on surface receptor concentrations (Section II B), $R_0^{(1)}$ and $S_0^{(1)}$ are replaced by $\psi - R_1^{(1)}$ and $\phi - S_1^{(1)}$, respectively. We then drop the subscripts from $R_1^{(k)}$ and $S_1^{(k)}$ to simplify notation.

$$\begin{aligned}
\partial_t R^{(1)} &= r_b L(\psi(x) - R^{(1)}) - (r_u + r_d^{(1)} + r_I^{(1)}) R^{(1)} + r_R^{(1)} R^{(2)} \\
\partial_t S^{(1)} &= \kappa_b L(\phi(x) - S^{(1)}) - (\kappa_u + \kappa_d^{(1)} + \kappa_I^{(1)}) S^{(1)} + \kappa_R^{(1)} S^{(2)} \\
&\;\;\vdots \\
\partial_t R^{(n_T)} &= r_I^{(n_T-1)} R^{(n_T-1)} - (r_R^{(n_T-1)} + r_d^{(n_T)}) R^{(n_T)} - \kappa_C R^{(n_T)} S^{(n_T)} + \kappa_S Q^{(n_T)} \\
\partial_t S^{(n_T)} &= \kappa_I^{(n_T-1)} S^{(n_T-1)} - (\kappa_R^{(n_T-1)} + \kappa_d^{(n_T)}) S^{(n_T)} - \kappa_C R^{(n_T)} S^{(n_T)} + \kappa_S Q^{(n_T)} \\
\partial_t Q^{(n_T)} &= \kappa_C R^{(n_T)} S^{(n_T)} - \kappa_S Q^{(n_T)}
\end{aligned} \tag{A2}$$

Note that we do not explicitly indicate the superscripts over chemical rate symbols when presenting the dynamical equations in the main text (Eq. 10-17) for simplicity of notation. In the numerical analysis, however, the degradation and internalisation-recycling rates of different tiers are treated separately.

The steady-state solutions of the above equations, without feedback controls on chemical rates, are given by

One-tier channel:

$$
\begin{aligned}
R^{(1)} &= \frac{r_b L}{r_b L + r_u + r_d^{(1)}}\psi \\
S^{(1)} &= \frac{\kappa_b L}{\kappa_b L + \kappa_u + \kappa_d^{(1)}}\phi \\
Q^{(1)} &= \frac{\kappa_C}{\kappa_S} R^{(1)} S^{(1)}
\end{aligned} \tag{A3}
$$

Two-tier channel:

$$
\begin{aligned}
R^{(1)} &= \frac{r_b L}{r_b L + r_u + r_d^{(1)} + \frac{r_d^{(2)} r_I^{(1)}}{r_R^{(1)} + r_d^{(2)}}}\psi \\
S^{(1)} &= \frac{\kappa_b L}{\kappa_b L + \kappa_u + \kappa_d^{(1)} + \frac{\kappa_d^{(2)} \kappa_I^{(1)}}{\kappa_R^{(1)} + \kappa_d^{(2)}}}\phi \\
R^{(2)} &= \frac{r_I^{(1)}}{r_R^{(1)} + r_d^{(2)}} R^{(1)} \\
S^{(2)} &= \frac{\kappa_I^{(1)}}{\kappa_R^{(1)} + \kappa_d^{(2)}} S^{(1)} \\
Q^{(2)} &= \frac{\kappa_C}{\kappa_S} R^{(2)} S^{(2)}
\end{aligned} \tag{A4}
$$

For channels with $n_T > 2$, the solutions are written in the following recursive form
Channel with n_T tiers:

$$
\begin{aligned}
R^{(1)} &= \frac{r_b L}{r_b L + r_u + \tilde{r}_d^{(n_T)}}\psi \\
R^{(k)} &= \frac{r_I^{(k-1)}}{r_R^{(k-1)} + \tilde{r}_d^{(n_T-k+1)}} R^{(k-1)} \quad \text{for } k = 2, 3, ..., n_T \\
S^{(1)} &= \frac{\kappa_b L}{\kappa_b L + \kappa_u + \tilde{\kappa}_d^{(n_T)}}\phi \\
S^{(k)} &= \frac{\kappa_I^{(k-1)}}{\kappa_R^{(k-1)} + \tilde{\kappa}_d^{(n_T-k+1)}} S^{(k-1)} \quad \text{for } k = 2, 3, ..., n_T \\
Q^{(n_T)} &= \frac{\kappa_C}{\kappa_S} R^{(n_T)} S^{(n_T)}
\end{aligned} \tag{A5}
$$

where $\tilde{r}_d^{(k)}$ are in turn evaluated recursively as

$$
\begin{aligned}
\tilde{r}_d^{(1)} &= r_d^{(n)} \\
\tilde{r}_d^{(n_T-k+1)} &= r_d^{(k)} \left(1 + \frac{r_I^{(k)}}{r_R^{(k)} + \tilde{r}_d^{(k+1)}} \frac{\tilde{r}_d^{(k+1)}}{r_d^{(k)}}\right) \quad \text{for } k = n_T - 1, n_T - 2, ..., 1 \\
\tilde{\kappa}_d^{(1)} &= \kappa_d^{(n)} \\
\tilde{\kappa}_d^{(n_T-k+1)} &= \kappa_d^{(k)} \left(1 + \frac{\kappa_I^{(k)}}{\kappa_R^{(k)} + \tilde{\kappa}_d^{(k+1)}} \frac{\tilde{\kappa}_d^{(k+1)}}{\kappa_d^{(k)}}\right) \quad \text{for } k = n_T - 1, n_T - 2, ..., 1
\end{aligned}
$$

However, the general form of Eq. A3-A5 holds upon introduction of inter-branch feedbacks (refer Fig. 5) and therefore the set of ODEs (Eq. A2) can be solved analytically by appropriately replacing the rates under feedback with the Hill-form functions discussed in Section II B. Cases with other types of feedbacks need to be solved numerically (Appendix C).

In writing these dynamical equations we have made two assumptions, simply as a matter of convenience. One may note that only the ligand bound states of receptors are transported between tiers. This is done with the consideration that residence times of unbound receptors within a compartment, other than the cell surface (first tier), is very small i.e. receptors in enclosed compartments re-bind the ligand quickly after unbinding due to small volume of the compartment. Further, the open loop control on receptors need not be strictly on surface receptors (tier 1). In principle, the control could be on the production rate of receptors. This does not change the solution in any substantial manner. For instance, in the case of two tiers, the solution would be

$$R_1^{(1)} = \frac{r_b L}{r_b L\left(1+\frac{r_I^{(1)}}{r_R^{(1)}+r_d^{(2)}}\right) + r_u + r_d^{(1)} + \frac{r_d^{(2)} r_I^{(1)}}{r_R^{(1)}+r_d^{(2)}}} \frac{r_p}{r_d^{(1)}} \tag{A6}$$

$$S_1^{(1)} = \frac{\kappa_b L}{\kappa_b L\left(1+\frac{\kappa_I^{(1)}}{\kappa_R^{(1)}+\kappa_d^{(2)}}\right) + \kappa_u + \kappa_d^{(1)} + \frac{\kappa_d^{(2)} \kappa_I^{(1)}}{\kappa_R^{(1)}+\kappa_d^{(2)}}} \frac{\kappa_p}{\kappa_d^{(1)}} \tag{A7}$$

and the rest of the species would follow hierarchically as in the case with surface receptor control. As long as the deviations in the denominator, $\frac{r_d r_I}{r_R+r_d}$ and $\frac{\kappa_d \kappa_I}{\kappa_R+\kappa_d}$ remain small compared to r_u, and $\psi \sim \frac{r_p}{r_d^{(1)}}, \phi \sim \frac{\kappa_p}{\kappa_d^{(1)}}$, the steady solutions for the two cases (control on surface receptors versus total receptors) will not differ significantly.

Appendix B: Heuristics and choice of feedback controls

The figure below illustrates the effect of feedback parameters in Eq. 18-19 discussed under Section II B.

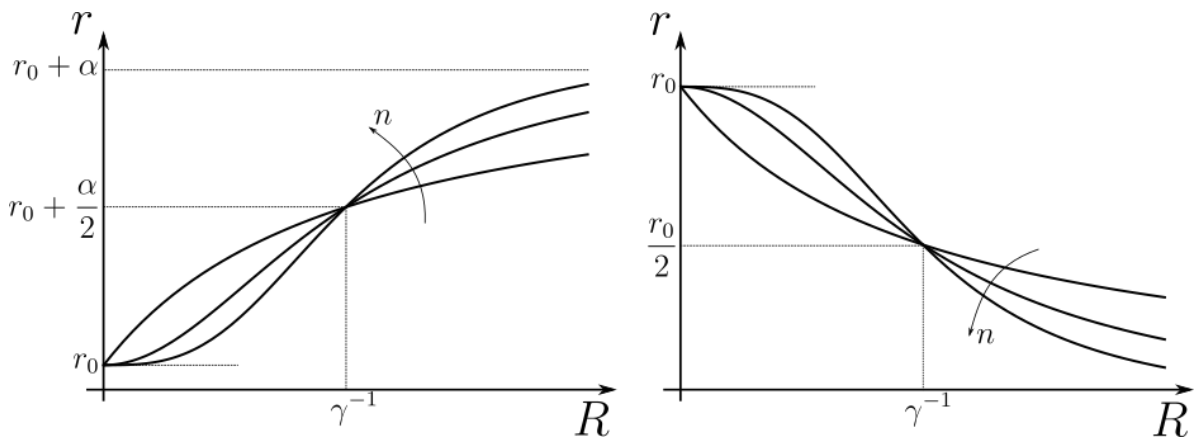

Figure 11. Hill functions representing positive (left) and negative (right) feedback control on chemical rates r actuated by chemical species R. The effect of feedback amplification α, sensitivity γ and strength n are indicated. r_0 denotes the reference value of the chemical rate r in absence of feedback.

Considering the choices of chemical rate under control $r \in \{r_I, r_R, r_d, \kappa_I, \kappa_R, \kappa_d\}$ and the actuating nodes $R \in \{R^{(1)}, R^{(2)}, ...\}$, there are a large number of possible feedbacks for any given channel architecture. However, categorising the different feedbacks according to their effect can reduce the redundancies and aid numerical analysis. The steady-state output of a channel without the feedback controls on chemical rates is instructive in this categorisation. For instance, consider the output θ for a two-tier two-branch channel with $n_T = 2$

$$\begin{aligned}\theta &= w_{n_T} Q^{(n_T)} + \sum_{k=1}^{n_T} w_k R^{(k)} \\ &= w R^{(1)} \left(1 + \frac{1-w}{w} \frac{r_I}{r_R+r_d}\left(1+\frac{\kappa_C}{\kappa_S}\frac{\kappa_I}{\kappa_R+\kappa_d} S^{(1)}\right)\right)\end{aligned} \tag{B1}$$

This form of the output suggests that feedbacks from $R^{(1)}$ (term outside the bracket) on any of the rates in $\frac{r_I}{r_R+r_d}$ and $\frac{\kappa_C}{\kappa_S}\frac{\kappa_I}{\kappa_R+\kappa_d}$ could cross-correlate $R^{(1)}$ with the other signalling species $R^{(2)}$ and $Q^{(2)}$. Thus, a negative feedback

on r_I (κ_I) would be qualitatively equivalent to a positive feedback on r_R (κ_R). Beside helping to reduce the number of CRNs that need to be considered, this observation also allows one to forego the numerical analysis of a CRN with feedback on r_R from $R^{(1)}$ that may have non-unique solutions. Similarly, feedbacks from different but related actuators could be interchanged. For example, the feedback on κ_I from $R^{(2)}$, i.e. $\kappa_I \to \frac{\kappa_I}{1+(\gamma' R^{(2)})^n}$, could be written in terms of the feedback on κ_I from $R^{(1)}$, i.e. $\kappa_I \to \frac{\kappa_I}{1+(\gamma R^{(1)})^n}$, by a simple transformation on feedback sensitivity $\gamma' = \frac{r_I}{r_R+r_d}\gamma$. Note that Eq. B1 also indicates the preferred direction of feedbacks, i.e. with the signalling receptors as actuators.

Appendix C: A note on numerical methods

Optimisation over the parameter vector $\vec{v}$ is in general non-convex. Moreover, the derivative of $\bar{\sigma}_X$ with respect to $\vec{v}$ is ill-defined due to finite sampling of input, and therefore, output distributions. With these considerations, we chose a derivative-free (gradient independent) optimisation algorithm viz. Pattern Search algorithm [63]. The implementation of this algorithm in MATLAB can be found as a function under the Global Optimization Toolbox. With this function, we perform the optimisation routine II C in two rounds. First with a certain number of initial points $n_{init} = 32$ to determine the feedback topologies (CRNs) that give lower global minima. In the next round, we go through the same optimisation routine for the feedback topologies obtained in the the first round but now with $n_{init} = 320$ to close in on the true global minimum. Using parallel computing clusters, the cost of this computation in terms of real running time can be brought down to 12-48 hours.

Ideally, this optimisation ought to be done with extrinsic and intrinsic noises considered together. However, we restrict optimisation to the case of extrinsic noise as the computational cost associated with steady-state solutions of chemical master equations (CMEs), in the case of intrinsic noise, is rather high. Therefore, we evaluate the inference error due to intrinsic noise only of those CRNs that were optimised in the context of extrinsic noise previously. For this, we solve the CMEs using adaptive explicit-implicit tau leaping algorithm [64] to determine the steady-state outputs and thus inference error. Implementation of this algorithm requires the definition of some numerical parameters that (i) help switch between Gillespie and implicit/explicit tau-leaping algorithms (n_a, n_d), (ii) decide the number of reactions when Gillespie algorithm is selected (n_b), and (iii) various threshold (n_c, ϵ). The values chosen for these are $n_a = 10$, $n_b = 10$ and $n_b = 100$ if implicit tau-leaping algorithm was used in the previous step, $n_c = 10$, $n_d = 100$, $\delta = 0.05$ and $\epsilon = 0.1$.

Appendix D: Robustness, Sensitivity and trade-offs

Precision in positional inference requires both that the output variance at a given position be small (i.e. the output is *robust* to the noise in input) and that the mean output at two neighbouring positions be sufficiently different (the output is *sensitive* to systematic changes in mean input).

With this heuristic understanding of an *ideal* output, we define two local measures: (i) χ measures the noise in the output of a cell cohort as compared to the noise in the received input. We define it as the ratio of coefficient of variation in the output θ to the coefficient of variation in the input L for the same cohort of cells

$$\chi \equiv \frac{\mathrm{CV}_\theta}{\mathrm{CV}_L}. \tag{D1}$$

Thus, *robustness* of the output increases with decreasing values of χ; (ii) ξ measures the *sensitivity* of the output to a systematic change in the input. We define it as the ratio of relative change in the mean output $\langle\theta\rangle$ to the relative change in the mean input μ_L for the same cell cohort

$$\xi \equiv \frac{\Delta\langle\theta\rangle}{\langle\theta\rangle} \Big/ \frac{\Delta\mu_L}{\mu_L} \tag{D2}$$

The angular brackets in the above equation denote averaging over cells belonging to the same cohort. Thus, higher *sensitivity* implies higher values of $|\xi|$. Precision in positional inference, in terms of these two local measures, implies simultaneous minimisation of χ and $|\xi|^{-1}$.

We calculate χ and ξ at all positions x in the various optimised channels. We find that addition of a branch allows for better robustness and alleviates the tension between sensitivity to systematic change in mean input and robustness to input noise (Fig. 13).

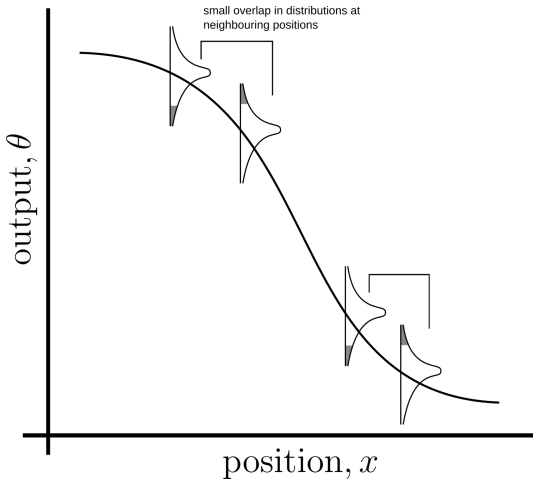

Figure 12. Schematic of an *ideal* output profile. The monotonically decreasing curve is the mean output profile. Due to various sources of noise, the output at any point will have a distribution around the local mean. If neighbouring cohorts of cells are to accurately distinguish their inferred positions from their outputs (in the Bayesian sense), the output distributions must have a small overlap (shaded region under the distribution curves).

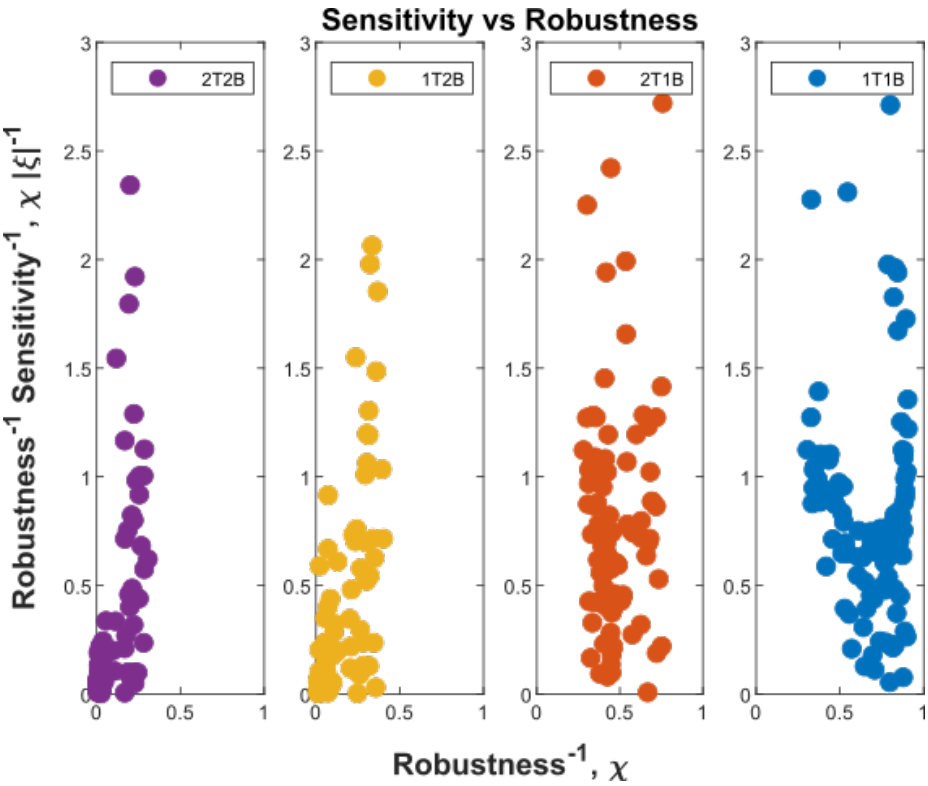

Figure 13. Robustness-Sensitivity plots for $n_x - 1 = 100$ cohorts in the optimised channel architectures. The robustness-sensitivity objective is to reach the origin along both the axes. Single-branch architectures (labelled 1T1B and 2T1B) show the two measures as conflicting objectives, such that improvement in robustness is achieved at the expense of sensitivity beyond a certain point. This conflict is absent in two-branch architectures (labelled 1T2B and 2T2B). An additional tier in two-branch architectures can further improve the two local measures. **Note:** the choice of coordinate axes reflects the requirement of simultaneous minimisation of χ and ξ^{-1} and the allowed tolerance in ξ^{-1} when χ is below a certain level.

Furthermore, a one-tier two-branch channel with an inter-branch feedback control (Fig. 7**a**) shows a preference towards certain concentrations of the two receptors, which provide the cellular output robustness to input noise, i.e. minimise χ. To maintain lower values of χ (higher robustness), the signalling receptors ψ must decrease with increasing mean of the input μ_L (Fig. 14). Increasing the non-signalling receptors ϕ as a function of mean input μ_L helps separate the mean outputs $\langle\theta\rangle$ at neighbouring positions and thus aids in increasing the sensitivity (Fig. 15). This is consistent with the receptor profiles in the optimised one-tier two-branch channel (Fig. 7**b**).

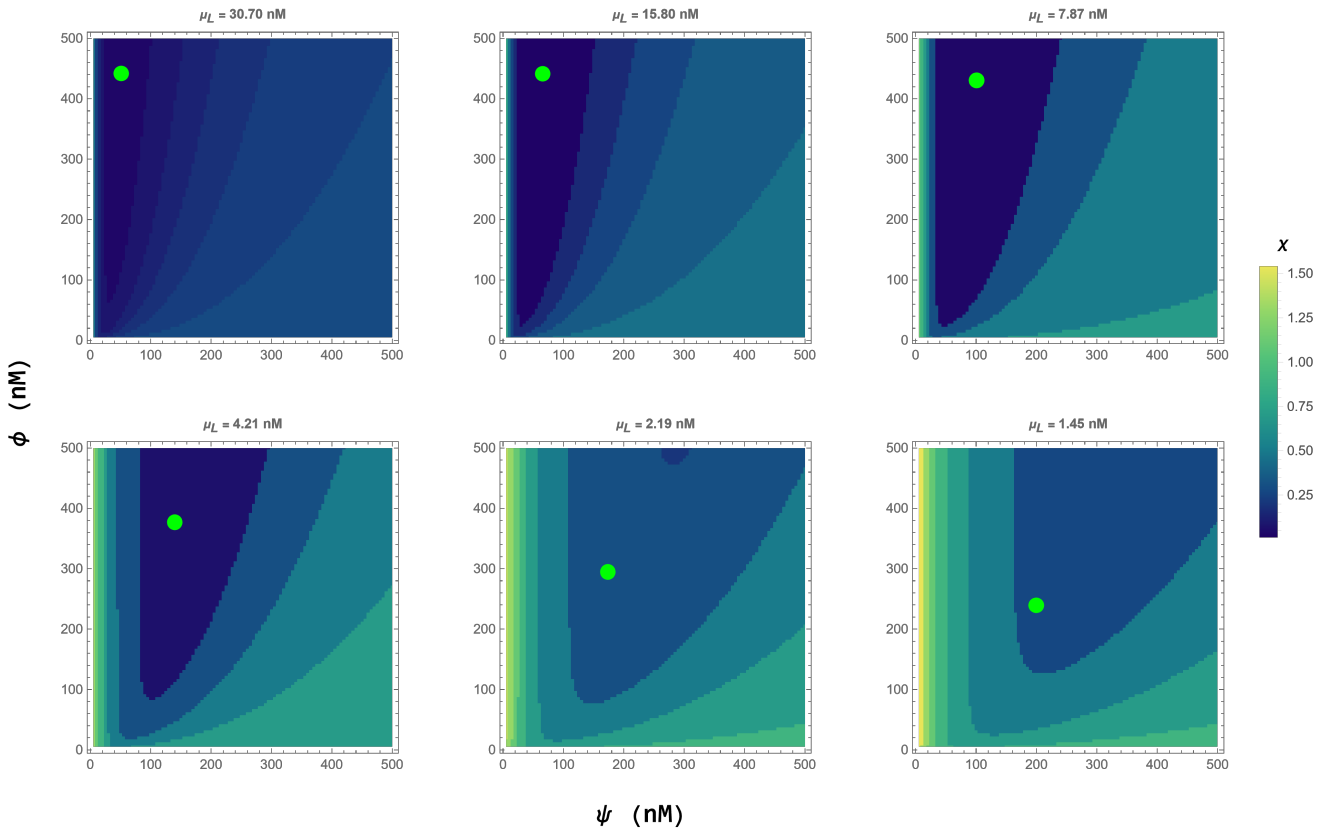

Figure 14. Contour plots of χ in a one-tier two-branch channel with inter-branch feedback control (Fig. 7**a**) showing the preferred receptor combinations (deep blue) for different values of mean input μ_L. Green dots denote the receptor concentrations in the optimised channel (Fig. 7**b,inset**) at positions corresponding to the values of mean input μ_L indicated above the contour plots. The optimised parameter values for the plots can be found in Table II under the column corresponding to $n_T = 1, n_B = 2, r_- = \kappa_C$.

Appendix E: Input-Output relations in a *minimal* channel

Before investigating the properties of various channel architectures in our study, we lay out some general results of a minimal channel with one tier and one branch. This channel "reads" the morphogen ligand input through binding of the ligand on only one, signalling receptor.

Fig. 16**a** shows that setting receptor concentrations to decrease with mean ligand input creates an unfavourable scenario. Low receptor availability for higher ligand concentrations ensures a saturation of the output at lower values (blue). On the other hand, higher receptor availability for low ligand concentrations is impractical as the output remains low despite increase in potential saturation point (purple). This causes large overlaps of the outputs at neighbouring positions. On the other hand, Fig. 16**b** shows that the output are better separated with receptor profiles that increase with the mean ligand input and thus would enable a better positional inference (Appendix D).

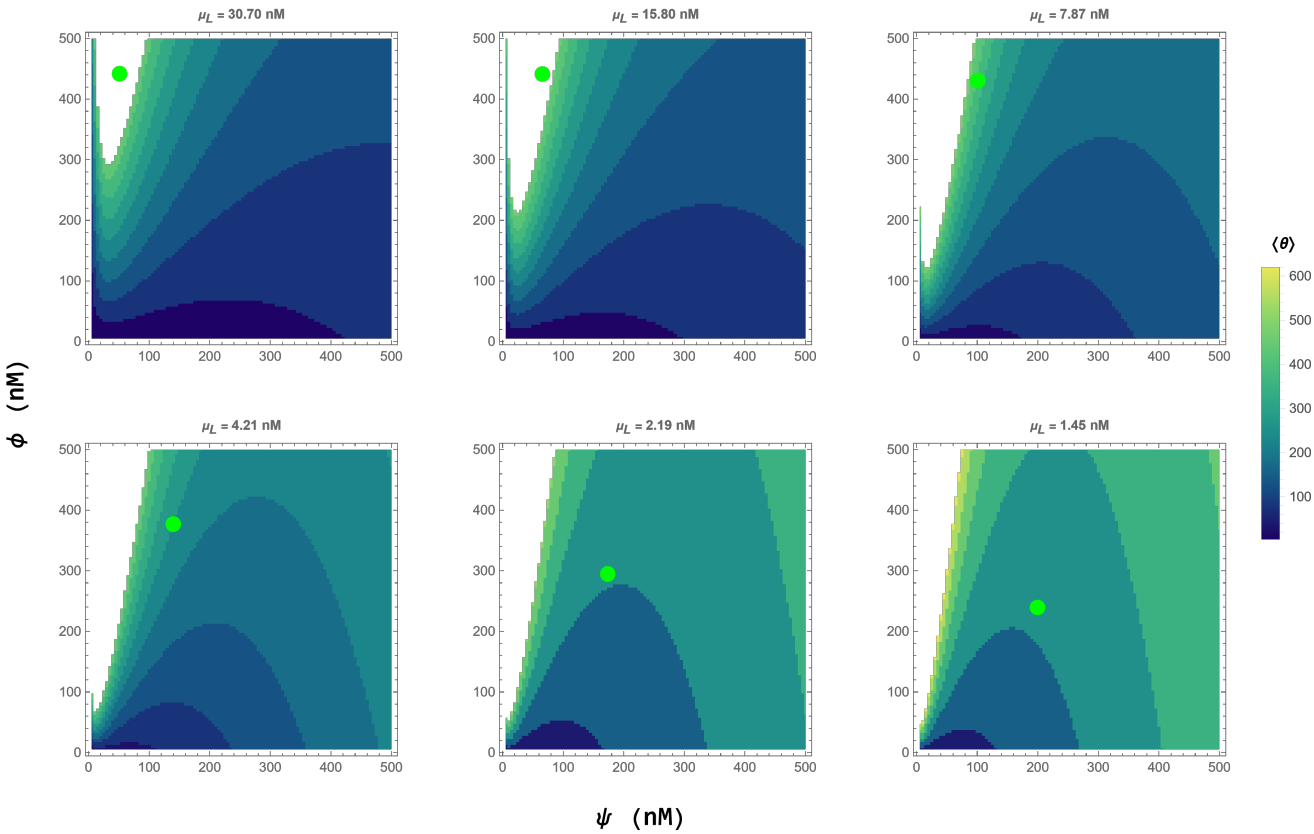

Figure 15. Contour plots of mean output $\langle\theta\rangle$ in a one-tier two-branch channel with inter-branch feedback control (Fig. 7**a**). The contours move downward along the axis of the non-signalling receptor ϕ. Therefore, as the preferred values of ψ decrease with input mean μ_L (Fig. 14), ϕ needs to increase with μ_L to ensure that the mean output $\langle\theta\rangle$ is a monotonically increasing function of μ_L. Green dots denote the receptor concentrations in the optimised channel (Fig. 7**b,inset**) at positions corresponding to the values of mean input μ_L indicated above the contour plots. The optimised parameter values for the plots can be found in Table II under the column corresponding to $n_T = 1, n_B = 2, r_- = \kappa_C$.

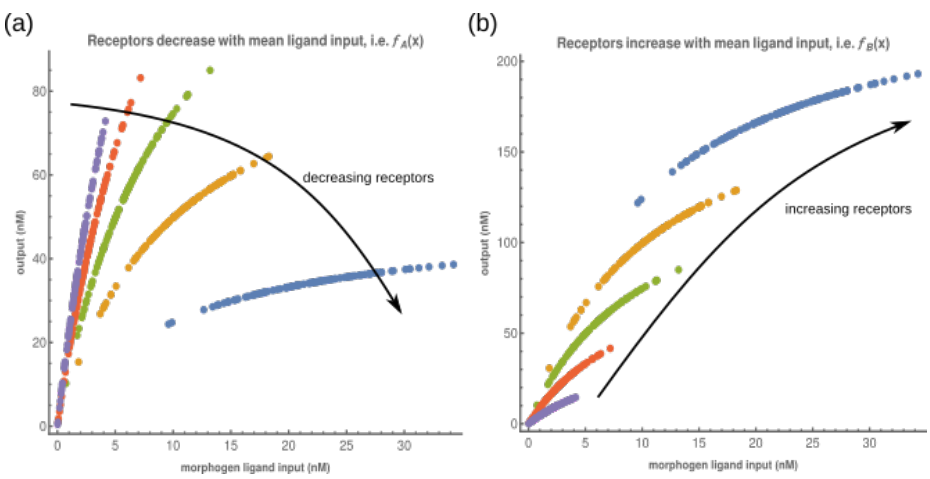

Figure 16. Input-Output function of a *minimal* channel shows the importance of choosing the correct receptor profiles.

Appendix F: Robustness due to inter-branch feedback

Here we describe the logic behind the working of an inter-branch feedback control. Consider the case of a one-tier two-branch channel with the feedback on conjugation rate κ_C actuated by the ligand bound state of the signalling receptor in the first tier $R^{(1)}$ (Fig. 7**a**). The steady-state solution to Eqs. 10-12 corresponding to this channel with $\kappa_C \to \frac{\kappa_C}{1+(\gamma R^{(1)})^n}$ is given by

$$R^{(1)} = \frac{r_b L}{r_b L + r_u + r_d}\psi \tag{F1}$$

$$S^{(1)} = \frac{\kappa_b L}{\kappa_b L + \kappa_u + \kappa_d}\phi$$

$$Q^{(1)} = \frac{\kappa_C}{\kappa_S}\frac{r_b L\psi}{r_b L + r_u + r_d}\frac{\kappa_b L\phi}{\kappa_b L + \kappa_u + \kappa_d}\frac{1}{1+\left(\gamma\frac{r_b L}{r_b L + r_u + r_d}\psi\right)^n} \tag{F2}$$

Therefore, the output can be expressed in terms of L, ψ and ϕ as follows

$$\theta = \frac{r_b L\psi}{r_b L + r_u + r_d}\left(1 + \frac{\kappa_C}{\kappa_S}\frac{\kappa_b L\phi}{\kappa_b L + \kappa_u + \kappa_d}\frac{1}{1+\left(\gamma\frac{r_b L}{r_b L + r_u + r_d}\psi\right)^n}\right) \tag{F3}$$

Fig. 17 describes the behaviour of the signalling species $R^{(1)}$ and $Q^{(1)}$ as given by Eq. F1,F2. $R^{(1)}$ increases monotonically with the ligand input L (blue curve, Fig. 17) and saturates at a value set by ψ. Meanwhile, the conjugate species $Q^{(1)}$ has a non-monotonic behaviour (yellow curve, Fig. 17): for very low values of input, $Q^{(1)}$ rises sharply due to absence of the feedback effect from negligible values of $R^{(1)}$, but then decreases with further increase in input as the value of the feedback actuator $R^{(1)}$ rises. This anti-correlated behaviour of $R^{(1)}$ and $Q^{(1)}$ results in the output $\theta \equiv R^{(1)} + Q^{(1)}$ being a more stable function of the input for an intermediate range of the input (region around the cusp in the green curve, Fig. 17). Modulating ψ and ϕ allows for placement of the stability region (cusp) in accordance with the range of ligand input received at any position x, thus tempering the noise in the output (see input-output relations in Fig. 8**d,h**).

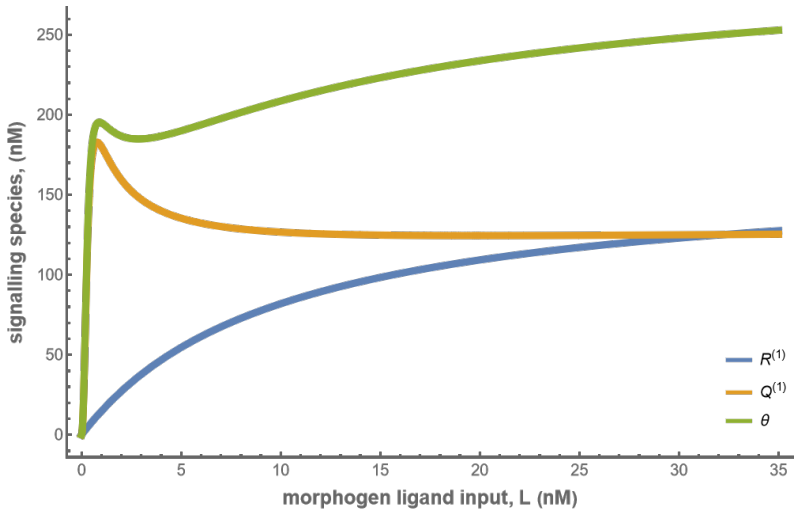

Figure 17. Concentrations of the signalling species $R^{(1)}, Q^{(1)}$ and total cellular output θ in the optimised one-tier two-branch channel with $\psi = 164\text{nM}, \phi = 318\text{nM}$. The optimised chemical rates and feedback parameters for the above plot can be found in Table II under the column corresponding to $n_T = 1, n_B = 2, r_- = \kappa_C$.

Appendix G: Reduction in inference errors due to extrinsic noise as a function of number of tiers

We find that the optimised average inference error $\bar{\sigma}_X$ decreases with the number of tiers n_T in a two-branch architecture with inter-branch feedback, albeit with diminishing returns. Here, we take up to three tiers in the channel architecture as the optimum $\bar{\sigma}_X$ saturates after $n_T = 2$ tiers.

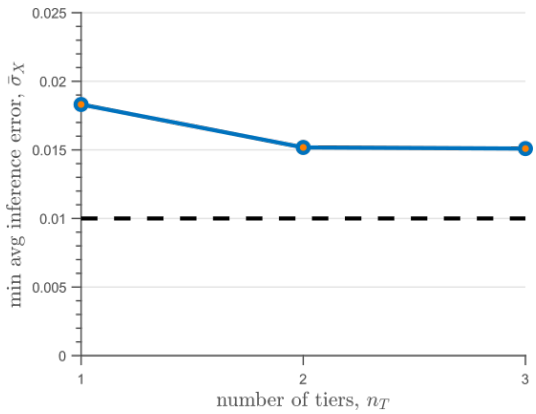

Figure 18. Optimised average inference error $\bar{\sigma}_X$ in two-branch architectures with increasing number of tiers n_T. The dashed line corresponds to a local inference error of one cell's width $\sim 1/n_x$.

Appendix H: Additional tiers dampen the effects of feedback to provide stability

Stochastic simulations of the CRN corresponding to the optimised one-tier two-branch channel (Fig. 9**a**) show large fluctuations in the time trajectories of chemical species $Q^{(1)}$ about its steady-state mean (Fig. 9 **d-f**). $Q^{(1)}$ increases due to absence of feedback from small values of $R^{(1)}$. However, beyond some amount of increase in $Q^{(1)}$, the trajectories go back towards their mean values. The state of small $R^{(1)}$ and increasing $Q^{(1)}$ can be maintained by replenishment of $R^{(1)}$ from binding reaction followed by immediate conjugation with large pools of $S^{(1)}$ due to high availability of the non-signalling receptor ϕ. Such fluctuations are absent in the two-tier two-branch channel (Fig. 9 **g-i**). Here, we discuss heuristics of the differing behaviours in the optimised one-tier and two-tier channels by taking a simpler set of CRNs (Fig. H) with the essential elements of these channels.

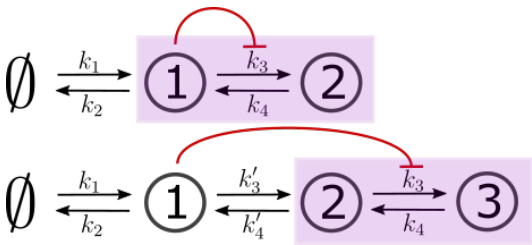

Figure 19. Two- and three-species CRNs with production k_1 and degradation k_2 rates of species 1 (s_1) and inter-conversion k_3, k_4 rates between the "signalling" (output generating) species (in purple box). These rates mimic the binding r_b, unbinding r_u and conjugation-splitting κ_C, κ_S rates respectively in the optimised one-tier two-branch and two-tier two-branch channels (Fig. 9**a,b**). Consistent with this mapping, the feedback is from species 1 on k_3. The three-species CRN has additional rates k_3', k_4' mimicking internalisation r_I and recycling r_R rates, respectively, in the optimised two-tier two-branch channel (Fig. 9**b**). In both cases, output is the sum of the last two nodes in the purple box.

The dynamics for the first, two-species CRN is given by

$$\begin{aligned} \dot{s_1} &= k_1(c - s_1) - (k_2 + k_3(s_1))s_1 + k_4 s_2 \\ \dot{s_2} &= k_3(s_1)s_1 - k_4 s_2 \end{aligned} \tag{H1}$$

and that of the second, 3-species CRN by

$$\begin{aligned}\dot{s_1} &= k_1(c - s_1) - (k_2 + k_3')s_1 + k_4' s_2 \\ \dot{s_2} &= k_3' s_1 - (k_4' + k_3(s_1))s_2 + k_4 s_3 \\ \dot{s_3} &= k_3(s_1)s_2 - k_4 s_3\end{aligned} \tag{H2}$$

with constant c playing the role of ψ, thus providing an upper bound to species 1. In both these sets of equations, we consider a feedback k_3 such that $k_3 \to \frac{k_0}{1+(\gamma s_1)^n}$ where k_0 represents the reference value of k_3 in absence of feedback. Fig. 20 shows the phase portrait for the dynamics of the 2-species CRN when $k_0 \gg k_1$ with a moderately strong feedback $n = 2$. This is representative of $\kappa_C S^{(1)} \gg r_b L$ in the optimised one-tier two-branch channel (Fig. 9**a**). The nullcline $\dot{s}_1 = 0$ (dashed, green curve) acts as a separatrix for the behaviour of this system: if due to fluctuations in species s_1 the system (s_1, s_2) crosses the nullcline from its steady-state (pink point), it sets out on a large trajectory (black line) such that s_1 remains close to zero while s_2 grows fast until the system turns back towards the steady state. This is similar to the trajectories of $R^{(1)}$ and $Q^{(1)}$ discussed earlier. The non-linearity of the separatrix is due to the feedback from s_1 on the rate k_3 that couples to s_1 in Eq. H1. Higher production rates k_1 (akin to higher values of ligand L in the optmised channel) bring the steady-state closer to the separatrix, making crossing of the separatrix due to fluctuations more likely. Having an additional node in between the actuator species and the controlled rate in the three-species CRN removes the non-linearity in $\dot{s}_1 = 0$ and provides buffering against this effect (Eq. H2).

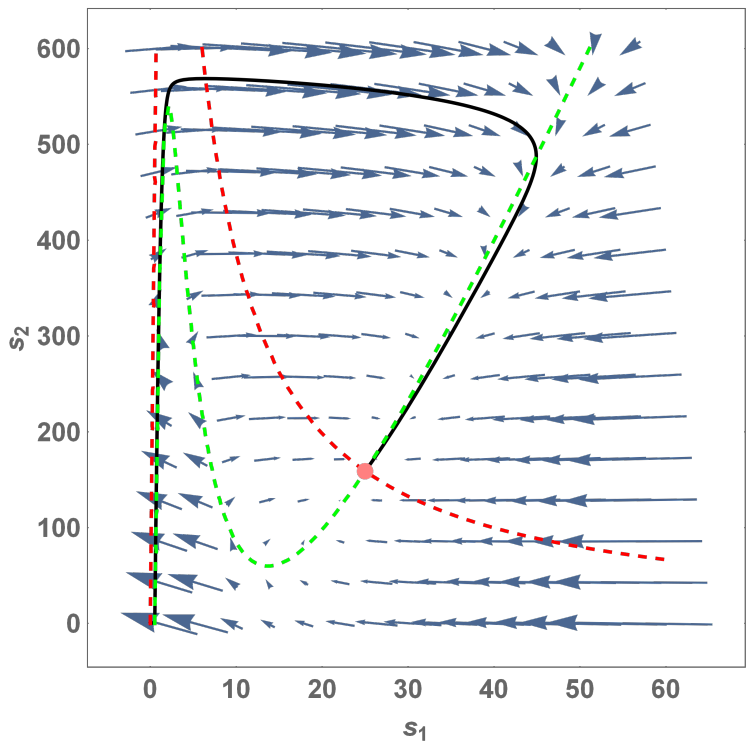

Figure 20. Phase portrait for Eqs. H1 with $k_0 \gg k_1$. The red and green dashed lines are the nullclines $\dot{s_2} = 0$ and $\dot{s_1} = 0$, respectively. The pink dot denotes the steady-state solution of this system. The solid black line is a trajectory with initial point at the origin. Note that at steady-state, $s_1 \ll s_2$. If s_1 drops beyond the green nullcline due to a fluctuation, the system goes back to the steady state through a long trajectory with s_1 essentially remaining close to zero for a long period of time while s_2 increases dramatically. Parameter values for the plot: $k_1 = k_2 = k_4 = 1, k_3 = 100, c = 50, \gamma = 0.5, n = 2$

Appendix I: Response in inference error due to perturbations in receptor concentrations

The definition of cellular output θ in a branched architecture involves making a distinction between the signalling and non-signalling receptors. In conjunction, the direction of the inter-branch feedback is from the signalling to the non-signalling branch (Fig. 8**a**). This gives rise to the possibility of an asymmetric response of the optimised channel to perturbations in the two receptors around the optimal point. Fig. 21**a** shows the average inference error $\bar{\sigma}_X$ due to the receptor profiles in Fig. 21**b,c** resulting from perturbations in the receptor control parameters A_2 and B_2 (Table I, Eqs. 8-9) around their optimal values. Each perturbed receptor profile (black curves in Fig. 21**b,c**) leads to a net deviation $\Delta\psi, \Delta\phi$ from the optimal receptor profile (blue curves in Fig. 21**b,c**), which is computed as follows

$$\Delta\psi = \int dx\ (\psi(x; A_2^* + \delta A_2) - \psi(x; A_2^*)) \tag{I1}$$

$$\Delta\phi = \int dx\ (\phi(x; B_2^* + \delta B_2) - \phi(x; B_2^*)) \tag{I2}$$

where A_2^* and B_2^* are the optimum values, and $\delta A_2, \delta B_2$ are the perturbations in the receptor control parameters. The local Hessian (curvature) of $\bar{\sigma}_X(\Delta\psi, \Delta\phi)$ around the optimal point ($\Delta\psi = \Delta\phi = 0$, red point in Fig. 21**a**) has eigenvalues $\lambda_1 \simeq 0.016, \lambda_2 \simeq 6.1$ corresponding to the eigenvectors that are nearly parallel to $\Delta\phi$ and $\Delta\psi$ axes, respectively (white arrows in Fig. 21**a**). This indicates that the inference error is much more sensitive to changes in the signalling receptor ψ than to changes in the non-signalling receptor ϕ, implying a *stiff* direction of control along the former and a *sloppy* direction of control along the latter.

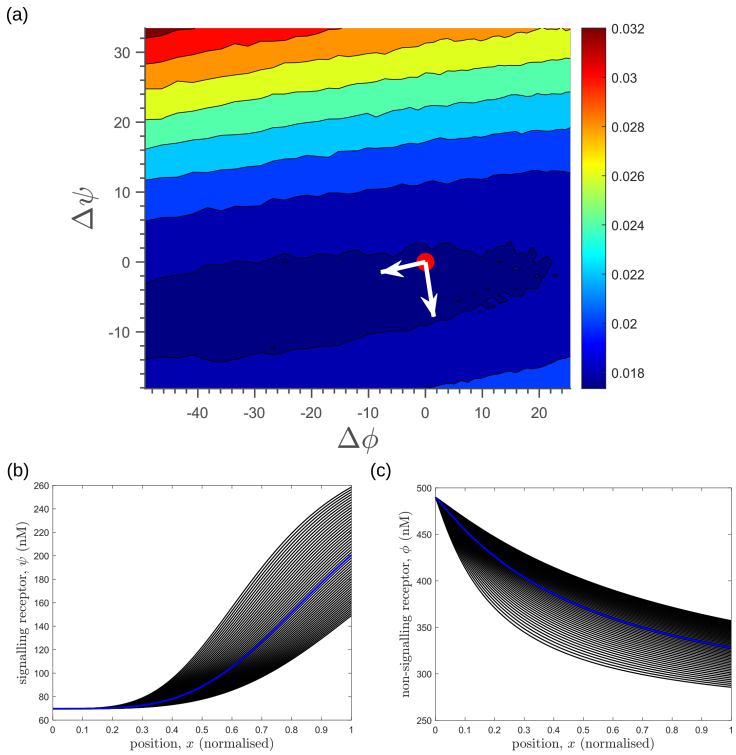

Figure 21. Response of average inference error in the optimised two-tier two-branch channel (Fig. 8**a**) to changes in receptor profiles shows the *stiff-sloppy* directions of control on receptors. **(a)** Contours of average inference error $\bar{\sigma}_X$ as functions of the net deviation from the optimal receptor profiles, as defined in Eqs. I1-I2. The white arrows indicate the directions of eigenvectors of the local Hessian (curvature) around the optimum (red point). The shorter arrow corresponds to the smaller eigenvalue (*sloppy* direction) while the longer arrow corresponds to the larger eigenvalue (*stiff* direction). **(b,c)** Perturbations in receptor profiles, $\psi(x)$ and $\phi(x)$ (black) around the optimal receptor profiles (blue). The optimised parameter values for the plots can be found in Table II under the column corresponding to $n_T = 2, n_B = 2, r_- = \kappa_I$.

Appendix J: Dependence of inference errors on input characteristics

The general qualitative features of the optimised channels remain invariant to changes in input characteristics. We find the same feedback topology and qualitative results when the one-tier two-branch channel architecture is optimised for input distributions with different decay lengths of mean input λ (Fig. 22). Lowering noise in the input, however, reduces the inference error of the optimised channel and extends the region of robustness in the tissue (Fig. 23).

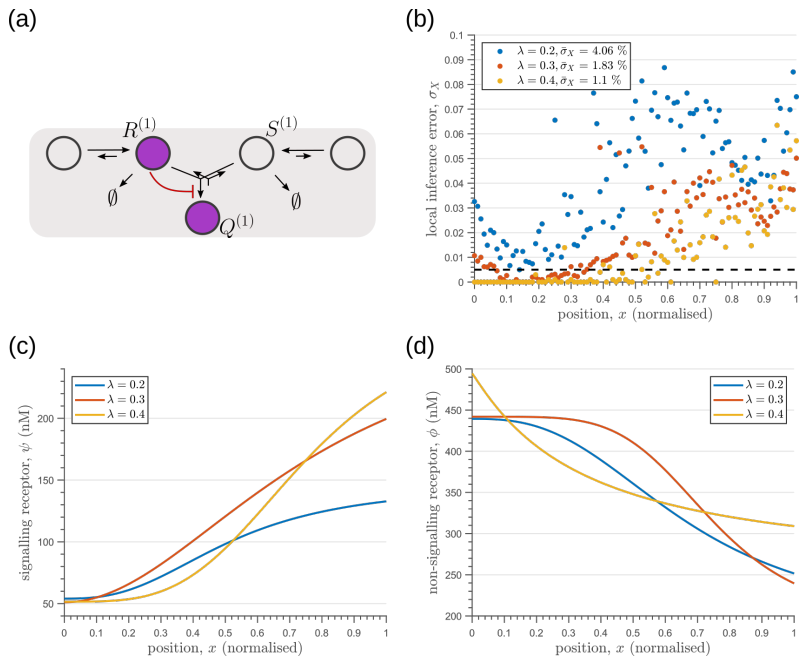

Figure 22. Optimisation of one-tier two-branch channels for extrinsic noise with varying mean input decay lengths λ (Eq. 2). **(a)** The channel architecture with inter-branch feedback shows the lowest inference error for all values of λ considered. **(b)** The minimum local and average inference errors decrease with λ. **(c)** Optimised profiles of the signalling receptors are increasing functions of x for the different values of λ. **(d)** Optimised profiles of the non-signalling receptors are decreasing functions of x for the different values of λ.

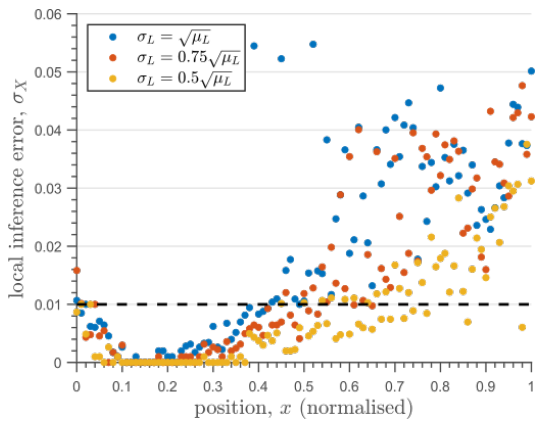

Figure 23. The one-tier two-branch channel optimised for input distribution with $\sigma_L = \sqrt{\mu_L}$ and $\lambda = 0.3$ shows smaller inference error for lower levels of input noise. The dashed line corresponds to a local inference error of one cell's width $\sim 1/n_x$. Note that the point at which local inference error departs away from 1% (one cell width error) extends further away from the source at $x = 0$.

Appendix K: Two-tier two-branch channel with no feedback

Here we show that the two-tier two-branch channel without an inter-branch feedback control has fundamentally different optimisation characteristics and a poorer positional inference.

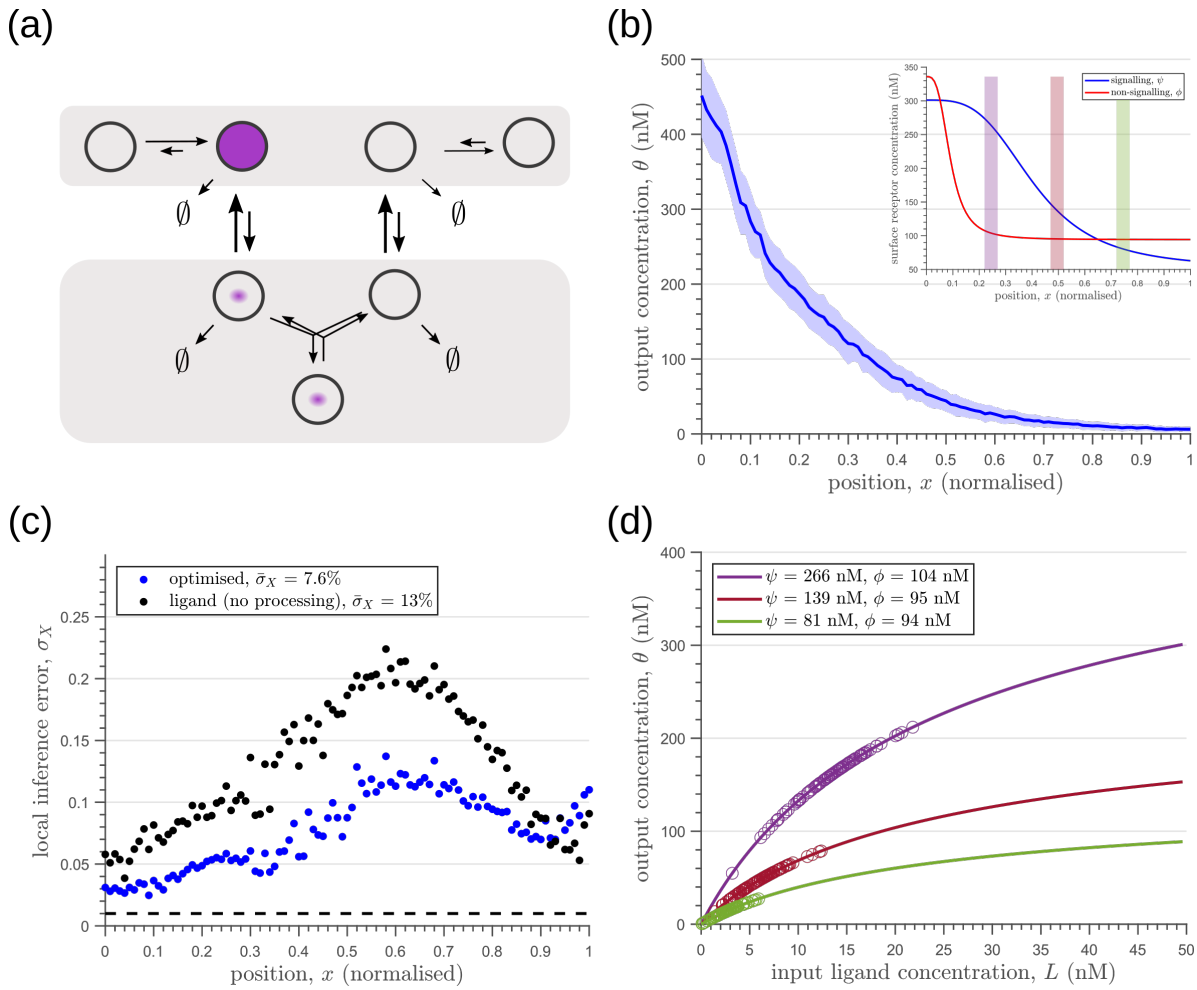

Figure 24. Results of optimisation of **(a)** two-tier two-branch channel with no feedback on rates. **(b)** The output profile (with standard error in shaded region) corresponding to the **(inset)** optimised signalling (blue) and non-signalling (red) receptor profiles. **(c)** The local inference error $\sigma_X(x)$ is only marginally reduced throughout the tissue, when compared to the expected inference errors from ligand with no processing. The dashed line corresponds to a local inference error of one cell's width $\sim 1/n_x$. However, **(d)** the input-output relations in this channel are restricted to monotonically increasing sigmoid functions saturating at only large values of input. The plots correspond to the receptor profiles at positions shaded with the same colour in (b, inset). The solid lines represent the input-output relation for the corresponding receptor combinations while the circles show the values of input-output pairs realised in the optimised channels. The optimised parameter values for the plots in (b-d) can be found in Table II under the column corresponding to $n_T = 2, n_B = 2, r_- = \{\}$.

Appendix L: Uniform receptor profiles with uncorrelated noise

Here we show that having spatially uniform profiles, with or without uncorrelated noise, for both the signalling and non-signalling receptors (Fig. 25**b,c**) leads to a higher inference error compared to the optimal (Fig. 25**a**). The inference error in these cases is comparable to a channel with no processing of the ligand (black dots in Fig. 25**a**). This provides the motivation for choosing monotonically increasing or decreasing receptor profiles (Eqs. 8-9), which

implicitly assume spatial correlations in the surface concentrations of receptors.

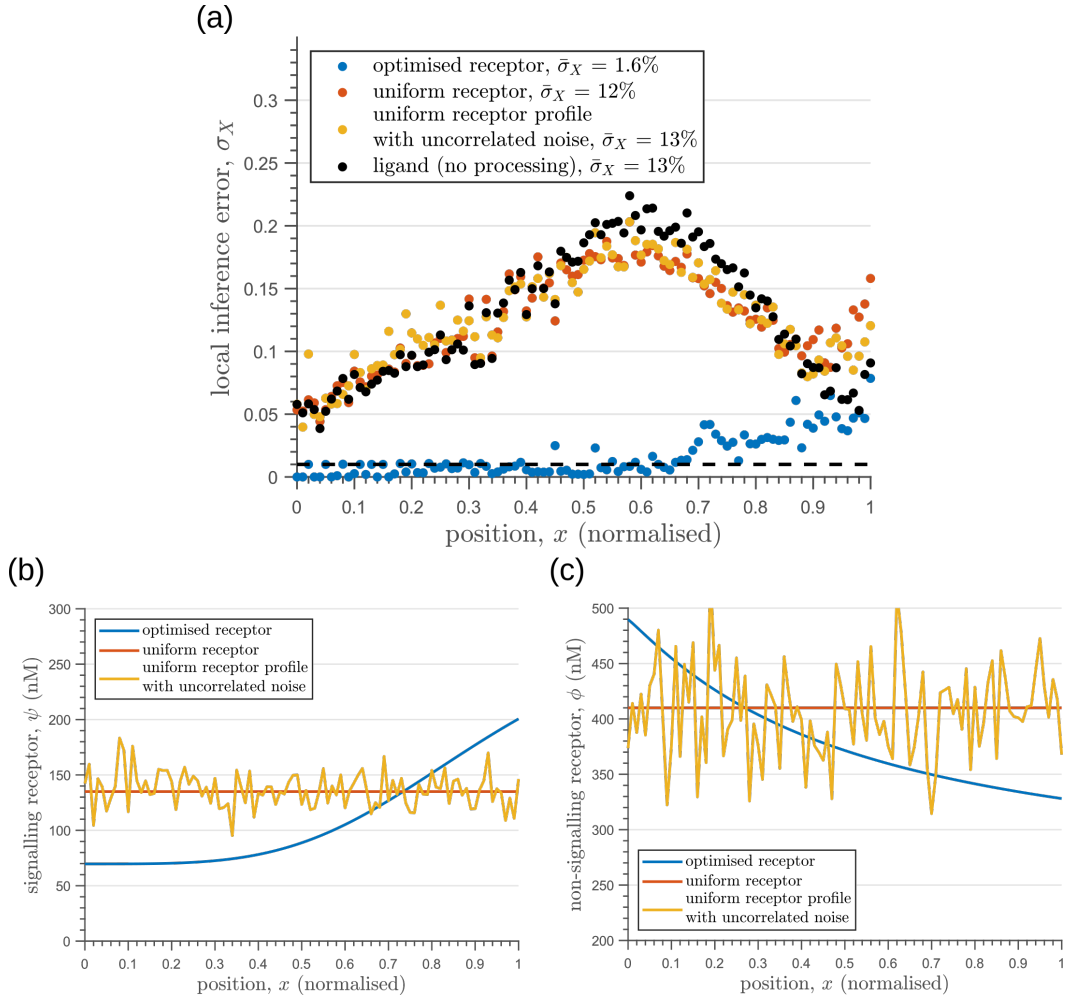

Figure 25. **(a)** Inference error profiles due to extrinsic noise in the optimised two-tier two-branch channels with optimal receptor profiles (blue), uniform receptor concentration (orange) and uniform receptor profiles with uncorrelated noise (yellow). **(b)** Signalling receptor profiles corresponding to the cases in (a). **(c)** Non-signalling receptor profiles corresponding to the cases in (a). In (b,c), the mean uniform receptor concentration is set to the mid point of the optimised receptor profile while the strength of the uncorrelated noise is 0.1 times the mean. The optimised parameter values for the plots in (a-c) can be found in Table II under the column corresponding to $n_T = 2, n_B = 2, r_- = \kappa_C$.

Appendix M: Experimental Methods

Fly stocks, endocytic assays, and imaging

Fly stocks used in this study are wildtype w1118, c5-GAL4, CAAX-GFP (Kyoto DGRC - 109823), Wg-GFP [65] and UAS-myr-Garz-E740K. Flies were reared on corn flour medium containing sugar, yeast and agar along with antibacterial and antifungal agents. Flies were grown in 25°C incubators with 12-hour light/dark cycles for experiments and otherwise maintained at 18°C or 22°C. Third instar larval wing discs were dissected in Graces live imaging media [66]. Dissected discs were incubated with labelled Wg antibodies (Wg-AF-568) on ice for 45 minutes. Discs were transferred to room temperature for indicated time of pulse, washed with ice cold 1XPBS buffer and fixed using 4% PFA (5 minutes on ice + 15 minutes at room temperature). Discs were then mounted in imaging chambers and imaged on a FV3000 laser-scanning confocal microscope using a 60X/1.42 NA oil objective (with acquisition XY pixel dimensions of $0.138\mu m$ and Z stacks of size $0.5\mu m$).

Analysis
The slice-by-slice images of the dome shaped wing disc from the confocal microscope were transformed into images from the outer most surface of the wing disc. This allowed us to compare the intensities of Wg from similar apico-basal height of cells across the dome-shaped epithelial. Wg production plane (Plane Q) and a perpendicular plane (Plane R) were defined. Intensity of different probes in curved tissues is affected by sample geometry and imaging depth. A data-based correction matrix was constructed using a uniform marker – CAAX GFP expressed uniformly under a ubiquitin promoter. Intensity for each disc, for each probe, was corrected using this data-based correction matrix. Detailed experimental and analysis methodology for extracting gradients from a curved tissue will be described elsewhere (Prabhakara C et al., in preparation). For computing the coefficient of variation - 18 bins parallel to Plane R were defined and intensities at different distances from the production plane was computed (schematic in Fig. 10**c**). Mean and standard deviation (SD) for each disc across multiple parallel bins at different distances from the producing cells x were used to estimate the coefficient of variation

$$\mathrm{CV}(x) = \frac{\mathrm{SD}(x)}{\mathrm{Mean}(x)} \tag{M1}$$

Computation of CV was done using intensity collected from the apical region of cells (20% of the entire length of cells). Normalized distance from the production plane is represented in all plots. Here, we have considered dorsal and ventral gradients to be equivalent.
Intensity profiles of endocytosed Wg

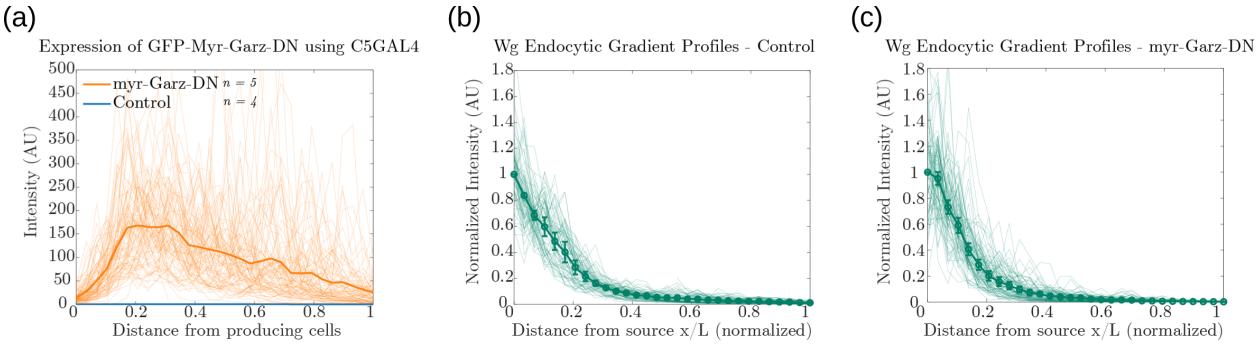

Figure 26. Fluorescence intensity profiles of: **(a)** GFP-Myr-Garz-DN and control. Endocytosed Wg profiles in **(b)** control wing discs (n=4) and **(c)** discs wherein CLIC/GEEC endocytic pathway is removed using UAS-myr-Garz-DN (n=5).

Table I. Parameters associated with rates, feedback and receptor profiles along with their range of values. The chemical rate values used in numerical analysis are scaled by the unbinding rate r_u, κ_u taken to be 1. The corresponding experimental values have been taken from Lauffenburger DA, Linderman JJ [47] where available.

Parameter	Symbol	Numerical values	Experimental values
Chemical rates			
Branch 1			
Unbinding rate	r_u	1	0.34 min^{-1}
Binding rate	r_b	0.1-1 nM^{-1}	0.072 $\text{nM}^{-1}\text{min}^{-1}$
Degradation rate	r_d	0.001-0.01	0.0022 min^{-1}
Internalisation rate	r_I	0.1-1	0.03-0.3 min^{-1}
Recycling rate	r_R	0.1-1	0.058 min^{-1}
Branch 2			
Unbinding rate	κ_u	1	-
Binding rate	κ_b	0.1-1 nM^{-1}	-
Degradation rate	κ_d	0.001-0.01	-
Internalisation rate	κ_I	0.1-1	-
Recycling rate	κ_R	0.1-1	-
Conjugation rate	κ_C	0.1-1 nM^{-1}	-
Splitting rate	κ_S	0.1-1	-
Feedback control			
Amplification	α	$0.1 - 10$	-
Feedback Sensitivity	γ	$0 - 1\text{nM}^{-1}$	-
Feedback strength	n	$0 - 5$	-
Receptor control			
Hill coefficient	a	$0 - 5$	-
Minimum concentration	A_0	$50 - 250\text{nM}$	-
Maximum concentration	$A_0 + A_1$	$50 - 500\text{nM}$	-
Position of half-maximum	A_2	$0.01 - 1$	-
Hill coefficient	b	$0 - 5$	
Minimum concentration	B_0	$50 - 250\text{nM}$	-
Maximum concentration	$B_0 + B_1$	$50 - 500\text{nM}$	-
Position of half-maximum	B_2	$0.01 - 1$	-
Ligand input			
Maximum concentration	A	30nM	-
Decay length	λ	$0.2 - 0.5$	-
Number of cells along x-direction	n_x	101	-
Number of cells along y-direction	n_y	101	-

Table II. Values of rates, feedback and receptor control parameters obtained after optimising the different channel architectures with n_T tiers and n_B branches. The optimised values of the chemical rates quoted below are scaled by the unbinding rate r_u, κ_u taken to be 1. The symbols r_- and r_+ denote positive and negative feedbacks, respectively, on the rates following the equals sign; {} implies absence of feedback.

Parameter (Symbol)	Value obtained in the optimised channel (n_T, n_B)				
	(1,1)	(1,2)	(2,2)	(2,2)	(2,2)
	$r_+ = r_d^{(1)}$	$r_- = \kappa_C$	$r_- = \kappa_I$	$r_- = \kappa_C$	$r_- = \{\}$
Chemical rates					
Branch 1					
Binding rate (r_b, nM^{-1})	0.0898	0.0949	0.0932	0.0893	0.0787
Degradation rate in tier 1 $(r_d^{(1)})$	0.0013	0.0081	0.0086	0.0098	0.0038
Degradation rate in tier 2 $(r_d^{(2)})$	-	-	0.0066	0.0087	0.0016
Internalisation rate (r_I)	-	-	0.0531	0.0784	0.0363
Recycling rate (r_R)	-	-	0.0681	0.0359	0.0758
Branch 2					
Binding rate $(\kappa_b, \mathrm{nM}^{-1})$	-	0.0590	0.0954	0.0835	0.0288
Degradation rate in tier 1 $(\kappa_d^{(1)})$	-	0.0086	0.001	0.0043	0.0068
Degradation rate in tier 2 $(\kappa_d^{(2)})$	-	-	0.0037	0.0031	0.0033
Internalisation rate (κ_I)	-	-	0.0741	0.0846	0.0559
Recycling rate (κ_R)	-	-	0.0123	0.0134	0.0998
Conjugation rate $(\kappa_C, \mathrm{nM}^{-1})$	-	0.9926	0.9823	0.9722	0.6019
Splitting rate (κ_S)	-	0.1285	0.1545	0.1350	0.7512
Feedback control					
Amplification (α)	3.2085	-	-	-	-
Feedback Sensitivity (γ)	0.2491	0.1831	0.5535	0.8259	-
Feedback strength (n)	2.6825	2.3683	2.0953	2.1880	-
Tier-wise weights					
weight of tier 1 (w_1)	1	1	0.0018	0.1232	0.9259
weight of tier 2 (w_2)	-	-	0.9982	0.8768	0.0741
Receptor control					
Hill coefficient (a)	4.9231	1.9974	3.8363	3.5251	3.3835
Minimum concentration (A_0, nM)	51.8130	51.0960	69.6940	51.9770	51.2
Maximum concentration $(A_0 + A_1, \mathrm{nM})$	298.283	290.356	304.114	134	301
Position of half-maximum (A_2)	0.4752	0.7818	0.9405	0.8344	0.4091
Hill coefficient (b)	-	4.8951	1.0802	1.7472	3.1821
Minimum concentration (B_0, nM)	-	192.32	248.69	192.4	94.1850
Maximum concentration $(B_0 + B_1, \mathrm{nM})$	-	442	489.77	441.67	305
Position of half-maximum (B_2)	-	0.7428	0.5177	0.3196	0.0902